



저작자표시-비영리-변경금지 2.0 대한민국

이용자는 아래의 조건을 따르는 경우에 한하여 자유롭게

- 이 저작물을 복제, 배포, 전송, 전시, 공연 및 방송할 수 있습니다.

다음과 같은 조건을 따라야 합니다:



저작자표시. 귀하는 원저작자를 표시하여야 합니다.



비영리. 귀하는 이 저작물을 영리 목적으로 이용할 수 없습니다.



변경금지. 귀하는 이 저작물을 개작, 변형 또는 가공할 수 없습니다.

- 귀하는, 이 저작물의 재이용이나 배포의 경우, 이 저작물에 적용된 이용허락조건을 명확하게 나타내어야 합니다.
- 저작권자로부터 별도의 허가를 받으면 이러한 조건들은 적용되지 않습니다.

저작권법에 따른 이용자의 권리는 위의 내용에 의하여 영향을 받지 않습니다.

이것은 [이용허락규약\(Legal Code\)](#)을 이해하기 쉽게 요약한 것입니다.

[Disclaimer](#)

공학박사학위논문

다공성 고분자의 팽창 및 용해 역학

Swelling and dissolution dynamics of porous polymers

2021 년 8 월

서울대학교 대학원

기계항공공학부

정 소 현

다공성 고분자의 팽창 및 용해 역학

Swelling and dissolution dynamics of porous polymers

지도교수 김 호 영

이 논문을 공학박사 학위논문으로 제출함

2021 년 4 월

서울대학교 대학원

기계항공공학부

정 소 현

정 소 현의 공학박사 학위논문을 인준함

2021 년 6 월

위원장 : 박형민

부위원장 : 김호영

위원 : 황원태

위원 : 선정운

위원 : 김원정

Swelling and dissolution dynamics of porous polymers

Sohyun Jung

Department of Mechanical and Aerospace Engineering
Seoul National University

A thesis submitted for the degree of

Doctor of Philosophy

August 2021

Abstract

Swelling and dissolution dynamics of porous polymers

Sohyun Jung

Department of Mechanical and Aerospace Engineering

The Graduate School

Seoul National University

With the recent development of hydrophilic, biodegradable, and stimulus-reactive polymers which can perform a specific function, the polymer widens its application scope into biomedical, soft robotics, and energy applications, so the research interest in a polymer is also growing. In this situation, as the depletion of fossil fuels and environmental problems are being magnified as serious threats to the survival of humanity, the study for eco-friendly functional polymers is emphasized. One method to endue a polymer with a specific function or improve the performance of functional polymers is utilizing the porous structure. The porous structure has the inherent characteristics of large surface area per unit volume, open channel, and tunability of the microstructure. Since the porous structure is eco-friendly in that this structure physically controls the polymer, the research interest in a porous polymer is growing. In many application cases, porous polymers encounter liquid-rich environments. When a porous polymer meets a liquid, the liquid

infiltrates into the porous polymer through its pores. In addition, the liquid can diffuse into the porous polymer through the polymer itself while deforming the porous polymer in two ways: swelling and dissolution. By utilizing the swelling and dissolution of porous polymers, the polymer system performing the necessary functions for specific applications can be developed. Besides, the physical properties of the porous polymer can be controlled. Here, we elucidated the mechanism of the swelling and dissolution of porous polymers by analyzing their dynamics and then develop functional polymer systems based on the findings. Firstly, we identified the swelling mechanism of the porous polymer, specifically electroactive hydrogel, according to the strength of the electric fields applied and devise the fast and powerful hydrogel actuator operated by the swelling of hydrogel. Secondly, we experimentally and theoretically investigated the dissolution dynamics of porous polymers according to the solubility of polymers. Based on our findings, we proposed a polymer system that can control the direction of dissolution in porous polymers by controlling the microstructure of porous polymers.

Keywords: Polymer, Porous media, Swelling, Dissolution, and Capillarity

Student Number: 2015-22723

Contents

Abstract	i
Contents	iii
List of Figures	v
List of Tables	xiii
1 Introduction	1
2 Swelling dynamics: Dynamics of electro-responsive strong hydrogel actuator	8
2.1 Introduction	8
2.2 Materials and methods	10
2.3 Characteristics of strong hydrogel actuators	12
2.4 Theoretical analysis	15
2.4.1 Stress generation dynamics without electric fields . .	15
2.4.2 Stress generation dynamics in electric fields	19
2.4.3 Maximum stress	25
2.5 Conclusion	27
3 Dissolution dynamics: Dynamics of soluble wicking	28
3.1 Introduction	28
3.2 Classification of soluble wicking regime	30
3.3 Partially soluble wicking	35
3.3.1 Experimental analysis	36

CONTENTS

3.3.2	Theoretical analysis	36
3.4	Completely soluble wicking	43
3.4.1	Experimental analysis	43
3.4.2	Theoretical analysis	44
3.4.3	Control the soluble flow direction	50
3.5	Conclusion	56
4	Concluding remarks	58
4.1	Summary of findings	58
4.2	Future works	61
A	Non-soluble wicking in directional porous sheets	63
	References	69
	Abstract (in Korean)	81

List of Figures

1.1	(a) A schematic of liquid imbibition into a capillary with a contact angle of zero under negligible effects of gravity. (b) A schematic of liquid imbibition into a porous medium.	2
1.2	(a) A schematic illustration of the pore size reduction during the swelling of porous polymer with constant apparent volume and (b) that of the increase in pore size to several pores merging into larger pores.	4
2.1	Schematic diagrams of the experimental apparatus used (a) to wrap a polyelectrolyte gel with a stiff and selectively permeable membrane and (b) to measure the force generated by swelling of a bare gel and a strong hydrogel actuator.	10

LIST OF FIGURES

- 2.2 (a) Images of the compression process of a fully swollen bare PSPA gel and (b) a fully constrained PSPA gel (a strong hydrogel actuator) with different kettlebells hanging from the force sensor and slowly lowered at 1 mm s^{-1} . The fully swollen bare hydrogel starts to deform at 35.9 N and completely collapses at 38.4 N, while the strong hydrogel actuator endures 188 N without noticeable deformation. (c) Images of a strong hydrogel actuator breaking a brick in only 5 minutes. (d) The force generated by a strong hydrogel actuator over time without electric fields. (e) The time for a 1 g bare gel to absorb 18 g of water in different electric fields from 0 to 1200 V m^{-1} . Inset: magnification of shaded region. (f) The maximum force generated by a strong hydrogel actuator before the actuator fails according to applied electric fields from 0 to 1200 V m^{-1} 13
- 2.3 Schematic of a hydrogel composed of polymer chains with sulfur functional groups that dissociate when the hydrogel, known as polyelectrolyte hydrogel, hydrates. During hydration, the bare polyelectrolyte hydrogel significantly expands its volume. The swollen hydrogel easily deforms at low compressive stress. When the polyelectrolyte hydrogel is encased in a stiff and selectively permeable membrane, this system, named a strong hydrogel system, cannot expand its volume as much as bare hydrogels during hydration. However, it can endure the large external stress without deformation. 14
- 2.4 (a) Osmotic water uptake mass of gels, m_o over time. (b) Osmotic water uptake mass of gels plotted according to eq. (2.6). 16

LIST OF FIGURES

- 2.5 (a) Osmotic actuating stress Ψ_m versus $\beta_o = Dc\Omega_l K A \Pi t / (RTV_m)$. The slope of the best-fitting line corresponding to $1/\delta$ is $1.4 \times 10^6 \text{ m}^{-1}$. (b) Osmotic actuating stress over time. The solid lines correspond to the theoretical osmotic actuating stress of the strong hydrogel actuator. The error bar is standard deviation of measurement values. 18
- 2.6 (a) The mass of swollen gels m_t in electric fields from $E = 0$ to 600 V m^{-1} . (b) Electroosmotic(EO) water uptake mass of gels m_e over time in electric fields ranging from 200 to 400 V m^{-1} . Inset: Electroosmotic(EO) water uptake mass of gels m_e in electric fields from 0 to 400 V m^{-1} at $t = 2000 \text{ s}$. (c) EO water uptake mass of hydrogels, plotting according to $\alpha_e Et$, where $\alpha_e = \rho \epsilon \zeta \phi A / \mu$. (d) The normalized maximum mass of swollen gels m_n according to electric fields from 0 to 600 V m^{-1} . The normalized maximum mass of swollen gel is obtained by dividing the maximum mass of a swollen gel at each electric fields to the maximum mass of a swollen gel in 600 V m^{-1} 20
- 2.7 (a) Electroosmotic (EO) actuating stress Ψ_p versus $\beta_e E$, where $\beta_e = \epsilon \zeta E \phi A t / (V_m \mu)$ and $t = 10 \text{ min}$. The slope of the best-fitting line corresponding to K is 9.2 kPa . (b) The total stress generated by strong hydrogel actuator over time in different electric fields such as 0 (circle), 100 (inverted triangle), 200 (square), 400 (diamond), and 600 V m^{-1} (triangle). 24
- 2.8 (a) The maximum stress generated by the strong hydrogel actuator without electric field $\sigma_{max,o}$ according to the ratio of the maximum volume of the membrane can envelop to the dry gel volume χ . (b) The maximum stress generated by the strong hydrogel actuator with electric fields ranging from 0 to 1200 V m^{-1} according to χ 26

LIST OF FIGURES

3.1	A schematic diagram of random deposition of electrospun fibers of PEO to produce a fibrous polymer sheet, and the corresponding SEM image of the sheet.	31
3.2	Properties of liquids used in the experiments at a temperature of 25°C. Symbols are also listed that appear in figures 3.5 and 3.9 indicating the experimental condition.	32
3.3	The dissolution rate of the porous PEO sheet according to the EG concentration. In the completely soluble wicking regime, PEO dissolves in the order of 10 s. In the partial soluble wicking regime, PEO does not fully dissolve even a week after.	33
3.4	(a) Propagation of liquid front against gravity into a strip of fibrous PEO. (b) Optical image of the completely soluble wicking and partially soluble wicking in fibrous PEO sheets. In the completely soluble wicking, a liquid quickly and largely dissolves a fibrous PEO sheet, so the connection between them disappears soon. However, in the partially soluble wicking, a liquid slightly dissolves a fibrous PEO sheet, then the connection between them remains even after a week. (c) Optical image of capillary imbibition of aqueous EG mixtures with various concentrations. In the image of concentrations of 0 to 60 wt%, t denotes the time taking until the sheet departs from the reservoir. In the image of concentrations 70 wt% and pure EG, t denotes the time we took the image. .	34
3.5	The time dependence of the square of the liquid invasion distance (L_p^2) of 70 wt% EG mixture and pure EG. The solid line indicates our model prediction. Inset: a plot with the vertical axis representing the invasion distance L_p	37

LIST OF FIGURES

3.6	(a) The environmental scanning electron microscope (ESEM, Philips XL-30 FEG) images of a PEO sheet before and after it imbibes 70 wt% EG mixture. The polymer fiber swells, and the fiber thickness becomes $1.2 (\pm 0.37)$ times greater than the initial value. (b) SEM images of the PEO sheet. The left image shows an initial PEO sheet, and the right shows a dehydrated PEO sheet after imbibing 70 wt% EG mixture. (c) Schematic illustration of liquid absorption through a tube with the radius R made of soluble material. The red dotted box represents the control volume for analyzing the dissolved PEO mass.	38
3.7	(a) The surface tension of 70 wt% EG mixtures versus PEO concentration (C) from 1 to 38 g L^{-1} . (b) Steady shear viscosity of 70 wt% EG mixture at a shear rate ranging from 1 to 100 s^{-1} and various PEO concentrations from 1 to 38 g L^{-1} . Symbols denote PEO concentration in g L^{-1} . (c) Dependence of the zero shear viscosity of 70 wt% EG mixture on. (d) An enlarged plot of the data for PEO concentration between 1 and 7 g L^{-1}	40
3.8	(a) Wicking of a liquid from a point source emanating from a capillary tube touching a PEO fibrous sheet. (b) Wicking of water in a randomly deposited soluble sheet. In (b), the up and down rows correspond to the flows from a point sourced (capillary) and a liquid pool, respectively.	44

LIST OF FIGURES

3.9 (a) The liquid invasion distance, L_s , of various liquids versus time in soluble porous sheets of randomly deposited PEO fibers. (b) L_s versus $\beta t/\mu$, plotted according to scaling law (3.8). (c) Schematics of physical processes during wicking of a porous sheet of randomly deposited soluble fibers. The solvent diffuses in fibers (orange arrows), which swell and turn to gel layer accordingly. The loosened polymer chains are dissolved away (yellow arrows) where they can meet fresh liquid, which becomes an instantaneously preferred direction of soluble wicking. (d) ESEM images of PEO fibers that swell and consequently buckle to contact with their neighbours under a high humidity. (e) Inverted microscopy image of a soluble random porous sheet being impregnated by water, whose wet area appears bright. 45

3.10 Schematic illustrations of solvent imbibition through a soluble capillary. (a) When the conduit is wide, the wicking velocity is an outcome of simultaneous interactions of capillary wicking, solvent diffusion into the wall, wall swelling, and dissolution. (b) When the conduit is narrow, the swelling polymer blocks the conduit rapidly. The wicking speed is determined by how fast the gel layer is dissolved into the liquid. (c) Schematics of pore clogging process in porous media, assumed as an assemblage of cylindrical conduits of equivalent radius R , due to solvent diffusion into polymeric wall. While the solvent diffuses into an inner wall of a single conduit by a distance ΔR , the conduit radius is reduced to $R - \delta$ due to the wall swelling as much as δ 47

LIST OF FIGURES

3.11 (a) Schematics of the gel layer formation in simply modelled porous sheet of randomly deposited soluble fibers. (b) Schematics of the location where the wicking resumes and stops. In the porous PEO sheets, the gel layer is retained in a direction having a microstructure of liquid diffusible so the wicking cannot resume, otherwise the wicking resumes. (c) Optical image of fully soluble wicking pattern and (d) Inverted microscopy image of it. 51

3.12 (a) Schematic illustration of the fabrication of the porous sheets composed of directionally aligned PEO nanofibers using electrospinning, and the corresponding SEM image. (b) Wicking of water in a soluble sheet composed of directionally deposited nanofibers. In (b), the up and down rows correspond to the flows from a point sourced (capillary) and a liquid pool, respectively. 53

3.13 (a) The liquid invasion distance, L_d , of various liquids versus time in soluble porous sheets of directionally deposited PEO fibers. (b) L_d versus $\beta t/\mu$, plotted according to scaling law (3.8). Schematics of physical processes during wicking in (c) the crosswise and (d) the lengthwise direction. (e) SEM images of a sheet of directionally deposited fibers after wicking of water emanated from a capillary. 55

A.1 (a) Random deposition of electrospun fibres of PEO, and the corresponding SEM image. (b) Directional deposition of electrospun fibres of PEO, and the corresponding SEM image. (c) Wicking of a liquid from a point source emanating from a capillary tube touching a PEO fibrous sheet. (d) Propagation of liquid front against gravity into a strip of fibrous PEO sheet. 64

LIST OF FIGURES

A.2 (a) The wicking distance of liquids A and B in insoluble porous sheets of randomly deposited fibres plotted according to (3.1). Inset: Raw data of L versus t . (b) The wicking distance of liquid A in insoluble sheets of directionally deposited fibres. Different power laws are observed depending on the flow direction. Inset: Linear plots of L_l and L_c versus t . (c) The wicking distances in insoluble sheets of randomly deposited fibres, and the lengthwise wicking distances in insoluble sheets of directionally deposited fibres, plotted according to scaling law (3.1). The slopes of the best fitting lines corresponding to $4k_r/\phi$ are 2.3×10^{-13} and 2.5×10^{-14} m² for random and directional substrates, respectively. (d) The crosswise wicking distance of liquids A and B plotted versus $\sigma Rt/\mu$ 67

List of Tables

3.1	Characteristics of the porous fibrous sheets. In fiber radius, std stands for standard deviation.	31
3.2	Characteristics of the porous fibrous sheets. In fiber radius, std stands for standard deviation.	53

Chapter 1

Introduction

Polymers, large molecules composed of various repeating structural units, are widely used in almost all industries for structures, such as a tire, textile, mechanical component, and platform, that require physical strength and chemical stability. With the recent development of hydrophilic, biodegradable, and stimulus-reactive polymers which can perform a specific function, the polymer widens its application scope into biomedical, soft robotics, and energy applications. In addition, as the depletion of fossil fuels and environmental problems are being magnified as serious threats to the survival of humanity, the study for eco-friendly functional polymers is emphasized. The porous structure has the inherent characteristics of large surface area per unit volume, open channel, and tunability of the microstructure. This porous structure is one of the methods to endue a polymer with a specific function or improve the performance of functional polymers (Wu *et al.*, 2019; Zhang *et al.*, 2018b). Since the porous structure is eco-friendly in that this structure physically controls the polymer, the interest in a porous polymer is growing.

The porous polymer has started to be commercially used in water treatment, the food industry, pharmaceutical industry, synthetic chemistry, petrochemical engineering, and environmental protection. The use of porous polymer is widened to Li-ion batteries and supercapacitors as separators.

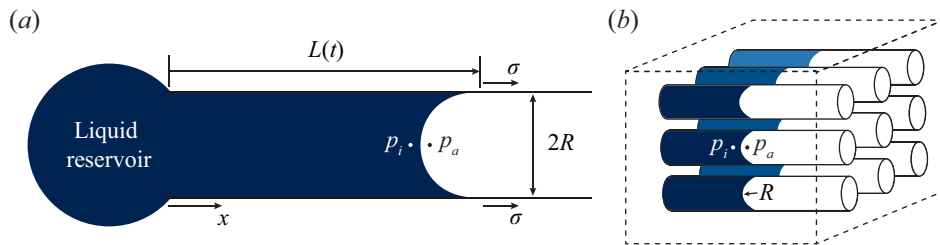


Figure 1.1: (a) A schematic of liquid imbibition into a capillary with a contact angle of zero under negligible effects of gravity. (b) A schematic of liquid imbibition into a porous medium.

In addition, porous polymers are promising in burgeoning fields such as gas adsorption/capture (Zeng *et al.*, 2016; Zou *et al.*, 2017), molecular separation (Carta *et al.*, 2013; Kim & Lee, 2015), catalysis (Puthiaraj *et al.*, 2016; Zhang & Riduan, 2012), electrochemical energy storage (Zhan *et al.*, 2017; Zhou & Wang, 2017), drug delivery (Fang *et al.*, 2015), sensors (Dong *et al.*, 2017; Gu *et al.*, 2014), and photo-energy conversion (Gu *et al.*, 2015, 2016). In many application cases, porous polymers encounter liquid-rich environments. When a porous polymer meets a liquid, the liquid infiltrates into the porous polymer through its pores and diffuse into the polymer chain networks while deforming the porous polymer in two ways: swelling and dissolution.

In case that the liquid is thermodynamically unstable with the polymer, the capillarity-assisted invasion of liquid in a porous polymer, referred to as wicking, happens without the deformation of polymer. The wicking dynamics are hard to be analyzed because of the critical complexity in the porous structure, so the theoretical attempts to understand the wicking dynamics have been made through the conceptual model approach (Scheidegger, 1958). The most general and simplest model representing a porous medium is a bundle of straight, parallel capillaries of uniform diameter. To analyze the wicking dynamics in this model, we first consider the velocity of the liquid front in a single wettable capillary of radius R , as shown in figure 1.1(a). The average velocity of incompressible liquid flow u in a small

axisymmetric straight capillary of radius R ($R \ll L$) follows the Poiseuille law written as $u = R^2(-dp/dx)/(8\mu)$ with L , μ , and p respectively being the propagation distance of the liquid, the viscosity, and the pressure. For the inertialess surface-tension-driven flow neglecting gravity, the pressure difference $\Delta p = p_a - p_i$, where p_a is the atmospheric pressure and p_i is the internal pressure at the liquid-gas interface. As the pressure of air just outside of the liquid-gas interface is also p_a , we realize that Δp is equal to the pressure jump across the interface, which is given by the Laplace-Young equation, $\Delta p = \sigma\kappa$ with κ being the interface curvature (de Gennes *et al.*, 2004). In a wettable capillary, $\kappa \approx 2R^{-1}$, and thus the average fluid velocity becomes $u = \sigma R/(4\mu L)$ (Lucas, 1918; Washburn, 1921). We now turn to total fluid flows in a bundle of capillaries embedded in a solid, as shown in figure porous(*b*). If N tubes are embedded in the unit cross-sectional area, then the total flow rate per unit cross-sectional area, q_m is $N\pi R^2 u$. Thus, we have $q_m = \phi R^2(-dp/dx)/(8\mu)$, where the porosity ϕ (a fraction of the volume of voids over the total volume) is $N\pi R^2$. The fluid flows in porous media with negligible inertia are described by Darcy's law (Bear, 1972; Darcy, 1856). For one-dimensional fluid flow, Darcy's law is written as $q_t = k/\mu(-dp/dx)$, which corresponds to the linear relationship between the total flow rate per unit area q_t and the pressure gradient, with k/μ being the prefactor. Here, k is the permeability. The analogy between q_m and Darcy's law is obvious. In q_m , $\phi R^2/8$ is analogous to the permeability k . In applying this relationship to the actual porous medium, R scales an average pore radius. The permeability k is highly related to the geometrical properties of pores, such as porosity, average size, size distribution, and shape of pores. Although the relationship between geometrical pore characteristics and permeability has long been under discussion through the empirical (Baver, 1949; Griffiths, 1952; Jacob, 1946; Nelson & Baver, 1941), and theoretical studies (Carman, 1941; Cornell & Katz, 1953; Kozeny, 1927; Purcell, 1949; Rose & Witherspoon, 1956), these attempts have only found the empirical relations for average permeability of porous media due to the

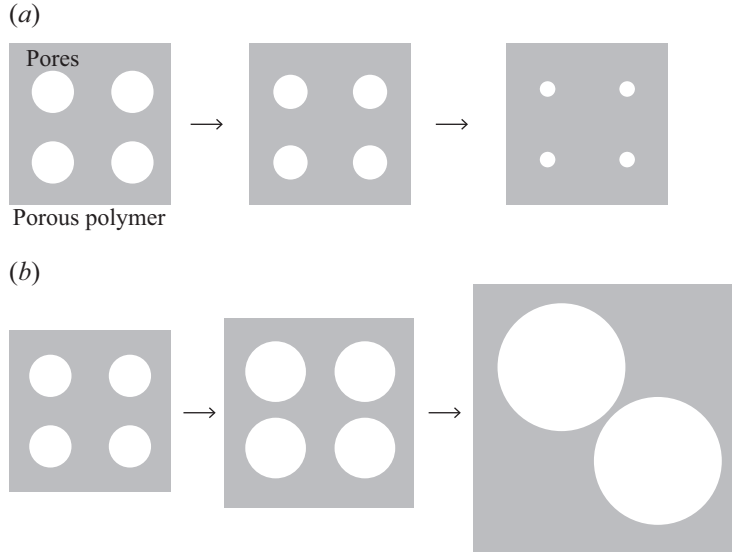


Figure 1.2: (a) A schematic illustration of the pore size reduction during the swelling of porous polymer with constant apparent volume and (b) that of the increase in pore size to several pores merging into larger pores.

complex nature of pore structure. To establish theoretical correlation, there is no other choice but to find the best model exhibiting the characteristic phenomena arising in a particular porous medium. Still, it is reasonable to scale the permeability as the cross-sectional area of actual fluid conduits.

When the liquid is thermodynamically stable with the polymer, the liquid diffuses into the polymer and either swells or dissolves it. In swellable porous polymers, liquid flow can expand the polymer while maintaining the apparent volume of the porous polymer. In this case, the pore size decreases as shown in figure 1.2(a), so the liquid flow rate decreases (Testoni *et al.*, 2018). However, the liquid flow in a swellable porous polymer also can expand the apparent volume and result in the pore size increase by the pore coalescence. Several pores are merged into a single large pore by the tension generated by the apparent volume increase as depicted in figure 1.2(b). Here, the liquid flow rate decreases due to the decrease in the capillary pressure, which results from the pore size at the wet front increase as

the liquid flow rate decreases (Ha *et al.*, 2018). In soluble porous polymers, the liquid which dissolves the polymer loosens the polymer chain network, causing the polymer to swell and separate the polymer chains from the bulk polymer. Therefore, the polymer dissolution process usually consists of the swelling step and the polymer chain disentanglement step. Depending on the governing step in polymer dissolution, porosity differently affects the dissolution rate of porous polymers. When the swelling is the governing step, the porosity has a positive relationship with dissolution rate (Colombo *et al.*, 1996). On the other hand, the porosity is independent of dissolution rate when the governing step is dissolution (Brielles *et al.*, 2007). Despite these pioneering but limited studies, the fundamental physical understandings of swelling and dissolution dynamics of porous polymers have rarely been attempted, so it is far from complete. However, it is of importance because the polymer system performing the necessary functions for specific applications can be developed and the physical properties of the porous polymer can be controlled by controlling the swelling and dissolution of the porous polymer.

This thesis aims to elucidate the mechanism of the swelling and dissolution of porous polymers by analyzing their dynamics and develop functional polymer systems. This thesis aims to elucidate the mechanism of the swelling and dissolution of porous polymers by analyzing their dynamics and develop functional polymer systems. In chapter 2, we identified the swelling mechanism of the porous polymer, specifically electroactive hydrogel, according to the strength of the electric fields applied and devise the fast and powerful hydrogel actuator operated by the swelling of hydrogel. Firstly, we observed the swelling dynamics of electroactive hydrogels within different electric fields by measuring the mass increase in the gel with time. Here, we found that the electroactive hydrogel without an electric field swells by osmosis, resulting in a significantly slow reaction rate. However, the gel within electric fields swells much faster and more than that without an electric field by electroosmosis which is the flow generated in the

porous media by the electric fields. Under the electric fields, the electroactive hydrogel swells faster as the electric fields become stronger. Utilizing this fast swelling electroactive hydrogel, we developed the fast and powerful hydrogel actuator. In this hydrogel actuator, the volume expansion of the gel is converted into internal stress in the gel by the stiff membrane wrapping the gel. The internal stress corresponding to the turgor pressure enhances the stiffness of the hydrogel actuator, so it allows the hydrogel to withstand or generate large forces. To derive the design parameters of this actuator for optimal design, we experimentally and theoretically analyzed the stress generated by the hydrogel actuator. The hydrogel actuator that we proposed is applicable in the manufacture of underwater structures or rescue equipment and has significance in overcoming the inherent weakness of the hydrogel, such as slow reaction and weak at compression. In chapter 3, we experimentally and theoretically investigated the dissolution dynamics of porous polymers according to the solubility of polymers. Based on our findings, we proposed a polymer system that can control the direction of dissolution in porous polymers by controlling the microstructure of porous polymers. Here, we evaluated the dissolution of porous polymers by observing the liquid invasion that dissolves the polymer. In porous media, the capillarity-assisted invasion of liquid, referred to as wicking, is occurred, so we study the dynamics of wicking accompanying the polymer dissolution, which we termed soluble wicking, in porous polymers. As a porous polymer, we used the fibrous porous sheets of polyethylene oxide(PEO) fabricated by electrospinning. PEO can be dissolved into water and chloroform but is insoluble in ethylene glycol and silicone oil, so we mix the water and ethylene glycol to control the PEO's solubility in liquids. We investigate the soluble wicking dynamics with the classification of the soluble wicking regime into partially soluble wicking and completely soluble wicking according to the PEO's solubility in liquids. In partially soluble wicking, we found that the porous polymer structure maintains despite the polymer dissolution, so the wicking mechanism is similar but slightly modified from

the insoluble wicking dynamics that is explained by Darcy's law. The rate of partially soluble wicking can be understood based on modified Darcy's law. However, the mechanism of the completely soluble wicking changes due to the disappearance of the medium's structure and the significant swelling of polymers. By the multi-scale visualization, we found that a gel layer was generated by the swelling of the polymer during the dissolution of porous polymers. This gel layer clogs the pores, so the capillary wicking through the pores is severely suppressed. However, the gel layer disappears soon by polymer chain disentanglement, and the capillary wicking through the pores is resumed. Thus, the completely soluble wicking is the repetitive process consisted of the pore-clogging step and the pore reopening step. From this mechanism that we elucidated, we obtained the theoretical model and demonstrated it by comparing the experimental results. Here, we theoretically found that completely soluble wicking can occur only in the direction where a liquid hardly diffuses into the porous polymer. Based on this finding, we proposed the microstructure for controlling the direction of dissolution in porous polymer by utilizing the inherent diffusivity difference according to the direction appearing in the fiber. We expected this dissolution direction control technology to use in controlled drug delivery, sensor, and a soft robot that transforms in response to the surrounding environment.

Chapter 2

Swelling dynamics: Dynamics of electro-responsive strong hydrogel actuator

2.1 Introduction

Hydrogels, the polymers composed of hydrophilic chain networks, absorb significant amounts of water within their interstices while maintaining the network structure in a swollen state. For decades the hydrogels have come into greater prominence and widened their applicable scope from optics to bioengineering, owing to their distinctive characteristics such as flexibility, hydrophilicity, swellability, biocompatibility, biodegradability, and stimuli sensitivity (Caló & Khutoryanskiy, 2015). However, the hydrogels are susceptible to compression due to their inherent low shear modulus and large Poisson's ratio, which limit their scope of applications (Chippada *et al.*, 2010). Besides, operation speeds of hydrogel in its applications are considerably slow because the swelling occurs by the passive transports of liquids represented by the diffusion. As the applicability of hydrogels to

soft robotics and soft actuators has emerged (Li *et al.*, 2021; Xiang *et al.*, 2021; Zheng *et al.*, 2021), many studies to improve its mechanical properties (de Ruijter *et al.*, 2018; Wu *et al.*, 2020; Xia *et al.*, 2013; Zhu *et al.*, 2017) and swelling rate (Chen & Park, 1999; Liu *et al.*, 2019; Xia *et al.*, 2013; Xu *et al.*, 2007; Yan *et al.*, 2005; Yan & Hoffman, 1995). To improve swelling rate, strategies have been mainly developed to introduce porous structures (Chen & Park, 1999; Liu *et al.*, 2019; Yan & Hoffman, 1995), micellar structures (Xu *et al.*, 2007; Yan *et al.*, 2005), or nanostructures (Xia *et al.*, 2013) to hydrogel have been mainly developed. All these strategies significantly improve the swelling rate of hydrogels, but most of them do not help improve mechanical properties. Only a few of these strategies improve the mechanical properties of hydrogels, even limited to elastic modulus (Li *et al.*, 2014; Xia *et al.*, 2013), not bulk modulus required to generate a large force.

Here, we report a novel strategy to improve the effective bulk modulus of hydrogels to generate large forces. By encasing the electro-active hydrogel with a stiff and semi-permeable membrane, we convert the swelling capacity of hydrogel into the internal stress that increases the effective bulk modulus of hydrogels. Thus, this hydrogel system, named a strong hydrogel actuator, can withstand and generate much greater stresses than a bare hydrogel. Furthermore, we accelerate the operating speed of a strong hydrogel actuator up to 585 times by applying an electric field on the hydrogel from 0 to 1200 V m^{-1} . The electric fields also increase the maximum stress of the strong hydrogel actuator. To derive the design parameters of this actuator for optimal design, we theoretically analyze the stress generation dynamics of strong hydrogel actuators by identifying the swelling mechanism of polyelectrolyte gel according to the presence of electric fields. Then, we predict the maximum generatable stress of a strong hydrogel actuator. The hydrogel actuator that we proposed is applicable in the manufacture of underwater structures or rescue equipment and has significance in overcoming the inherent weakness of the hydrogel, such as slow reaction and

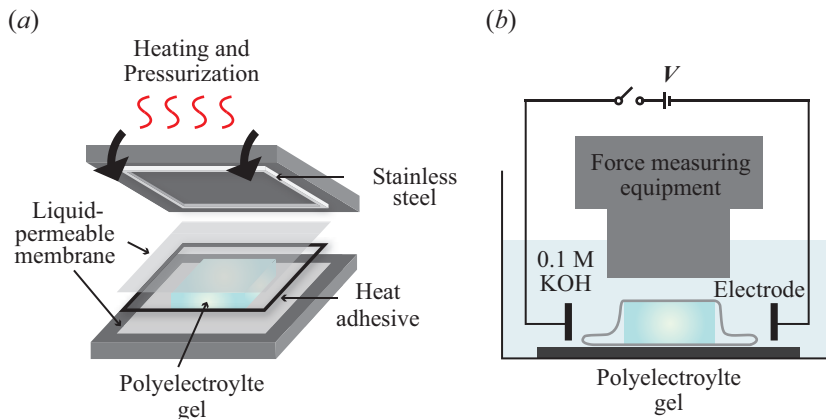


Figure 2.1: Schematic diagrams of the experimental apparatus used (a) to wrap a polyelectrolyte gel with a stiff and selectively permeable membrane and (b) to measure the force generated by swelling of a bare gel and a strong hydrogel actuator.

weak at compression.

2.2 Materials and methods

Hydrogel preparation To synthesize 3 M poly(3-sulfopropyl acrylate potassium salt) (PSPA) gel, we used 3-Sulfopropyl acrylate potassium salt (SPA; Sigma-Aldrich 251631) as the monomer of the polyelectrolyte gel network and N, N-methylenebisacrylamide (MBAAm, Sigma-Aldrich M7279) as the cross-linking agent, and Lithium phenyl-2,4,6-trimethylbenzoylphosphinate (LAP, Sigma 900889) as a photoinitiator for gelation. All chemical reagents were used without further purification. We blended cross-linker MBAA and initiator LAP with 3.0 M SPA. The cross-linker MBAA and initiator LAP have ratios of 2.1×10^{-3} and 6.7×10^{-5} to the moles of the SPA monomer, respectively. We poured this mixture into an acrylic mold followed by 365 nm UV irradiation (CL-1000L UVP) for 10 minutes.

Fabrication of strong hydrogel actuator We cut selectively permeable membranes, which are dishcloths composed of the rayon and polyester

2.2 Materials and methods

blend (Sunwooland 636255708), with a LASER cutting machine (Universal LASER system VL3.50) and placed it on the plate. We put the synthesized PSPA gel on the permeable membrane and laid another permeable membrane with a thermal adhesive sheet (Wappenshop 692027683) upon the gel as shown in figure 2.1 (a). Then, we covered it with stainless steel cover and applied heat and pressure. The fabricated sample was kept in a humid chamber to prevent the gel from drying before characterization. We term this fully encased PSPA gel as a strong hydrogel actuator henceforth.

Swelling rate measurement of gels We measure the swelling rate of electro-actuated hydrogel to analyze the expansion of the gel with and without the electric field. For this, we placed an electro-responsive hydrogel with a volume of 25 mm x 8 mm x 4 mm in the middle between the two platinum electrodes of size 3 cm x 5 cm that are in an acrylic chamber filled with deionized water. A voltage was applied with a DC power supply (KEYSIGHT E36233A) to Pt electrodes with a 5 cm gap between electrodes. We measure the swelling rate of a hydrogel by weighing the mass of hydrogel at specific time intervals.

Force measurement generated by hydrogels and strong hydrogel systems To measure the force generated by swelling of a bare gel and a strong hydrogel actuator, we placed two types of gel under the force measuring equipment (100 kN load cell; Instron 5582) with a distance of 4 mm, as depicted in figure 2.1(b). One is the hydrogel in the naked state, and the other is the hydrogel wrapping the two 40 mm x 23 mm membrane. Both hydrogels have a size of 25 mm x 8 mm x 4 mm. The area in which the force measuring instrument contacts the sample is 30 mm x 60 mm. We placed a hydrogel with force measuring instrument halfway between two submerged Pt electrodes in 0.1 M electrolyte solution composed of Potassium hydroxide pellet (KOH; Sigma P1767) and deionized water. We measured the force generated by the strong hydrogel actuator over time with various electric fields from 0 to 600 V m⁻¹.

2.3 Characteristics of strong hydrogel actuators

Hydrogels are generally susceptible to compression due to their inherent low shear modulus and large Poisson's ratio. Among the various hydrogel, we use 3 M PSPA gel corresponding to a special class of hydrogels known as polyelectrolyte gel. To test the durability of the PSPA gel against compressive forces, we slowly pressed it with a 4 kg kettlebell connected to a force sensor as shown in figure 2.2(*a*). The gel starts to deform at 35.9 N and completely collapses at 38.4 N. However, the geometrically fully constrained PSPA gel, which is termed strong hydrogel actuator, withstands much greater forces than the bare hydrogel. Here, we fully confine the gel by encasing the gel with a stiff and selectively permeable membrane having a smaller size than the fully swollen hydrogel (see Figure 2.3). Strong hydrogel actuator maintains its form even at 188 N of compressive force as shown in figure 2.2(*b*) and generate a large force enough to break bricks while swelling (see Figure 2.2(*c*)). By measuring the force generated by a strong hydrogel actuator over time, we also find that the strong hydrogel actuator becomes powerful as it expands (see Figure 2.2(*d*)). Since polyelectrolyte gels are composed of a crosslinked polymer network with ionizable functional groups, the electric field can act as a stimulus that affects its swelling behavior. Here, we apply electric fields and measure the time until the 1 g of bare PSPA gel absorbs 18 g of water within electric fields from 0 to 1200 V m^{-1} . The electric fields accelerate the response time of the gels a maximum of 585 times, as shown in figure 2.2(*e*). Furthermore, the electric fields increase the maximum generated force by the strong hydrogel actuator (see Figure 2.2(*f*)). The force is measured only before the actuator fails, so the maximum force represents the maximum value before the system fails.

2.3 Characteristics of strong hydrogel actuators

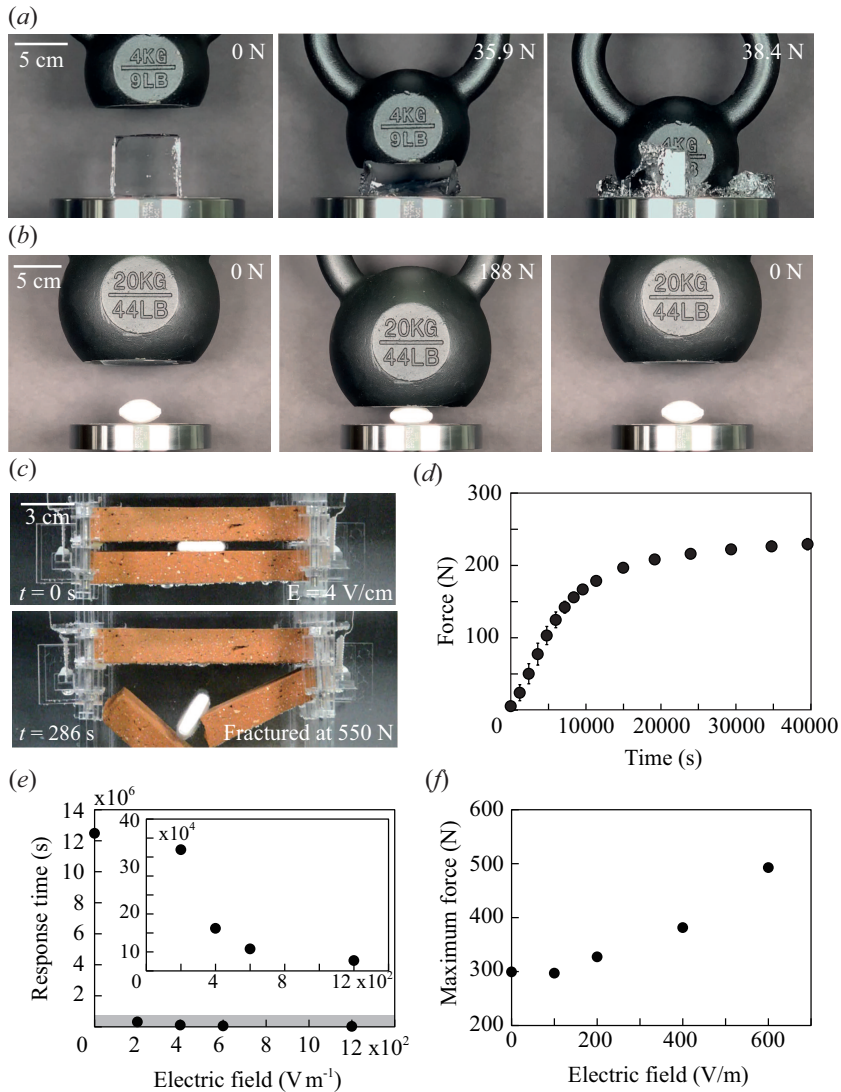


Figure 2.2: (a) Images of the compression process of a fully swollen bare PSPA gel and (b) a fully constrained PSPA gel (a strong hydrogel actuator) with different kettlebells hanging from the force sensor and slowly lowered at 1 mm s^{-1} . The fully swollen bare hydrogel starts to deform at 35.9 N and completely collapses at 38.4 N, while the strong hydrogel actuator endures 188 N without noticeable deformation. (c) Images of a strong hydrogel actuator breaking a brick in only 5 minutes. (d) The force generated by a strong hydrogel actuator over time without electric fields. (e) The time for a 1 g bare gel to absorb 18 g of water in different electric fields from 0 to 1200 V m^{-1} . Inset: magnification of shaded region. (f) The maximum force generated by a strong hydrogel actuator before the actuator fails according to applied electric fields from 0 to 1200 V m^{-1} .

2.3 Characteristics of strong hydrogel actuators

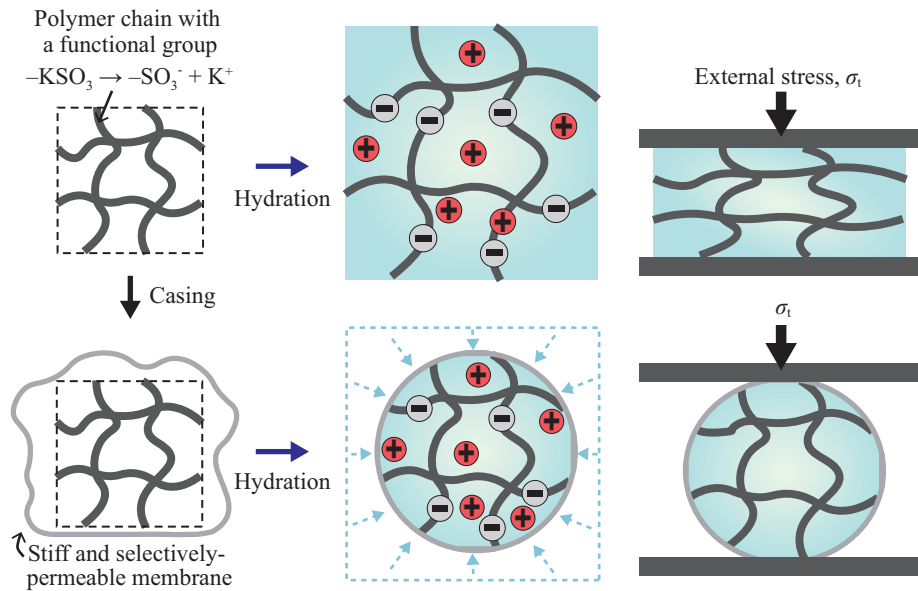


Figure 2.3: Schematic of a hydrogel composed of polymer chains with sulfur functional groups that dissociate when the hydrogel, known as polyelectrolyte hydrogel, hydrates. During hydration, the bare polyelectrolyte hydrogel significantly expands its volume. The swollen hydrogel easily deforms at low compressive stress. When the polyelectrolyte hydrogel is encased in a stiff and selectively permeable membrane, this system, named a strong hydrogel system, cannot expand its volume as much as bare hydrogels during hydration. However, it can endure the large external stress without deformation.

2.4 Theoretical analysis

2.4.1 Stress generation dynamics without electric fields

When a bare polyelectrolyte gel is hydrated as shown in figure 2.3, the volume of the gel expands as much it uptakes the water because the polymer networks and the water are incompressible (Hu *et al.*, 2010). Here, the total volumetric stain of the gel γ_t is equal to the volumetric hygroscopic swelling strain, γ_h , so the gel is stress-free, and the swollen polymer networks withstand all external stress. However, once the gel is fully confined by a stiff membrane and fills the inside of the membrane as shown in figure 2.3, the gel can no longer expand. Then, $\gamma_t = \gamma_h + \gamma_p = 0$, so $\gamma_p = -\gamma_h$, with γ_p being the volumetric mechanical strain that generates the internal stress σ_p in the gel. The internal stress developed by hydration follows Hooke's law, $\sigma_p = K\gamma_h$ with K being the bulk modulus of the hydrogel (Lin *et al.*, 2009). Because hydrogels swell as much as they absorb water, $\gamma_h = V_w/V_m$, where V_w and V_m are the water absorb the volume of hydrogels after the hydrogel filled inside the membrane and the maximum volume of the stiff membrane can wrap, respectively. The volume of water uptake is the summation of net flow rate into the gel over time t , so the internal stress produced by hydration is given as:

$$\sigma_t = K \frac{\int_0^t Q_n dt}{V_m}, \quad (2.1)$$

where Q_n is the net flow rate into the gel. Since the internal stress withstands external stresses with the swollen polymer networks, the effective bulk modulus of fully confined gel increases, and the fully confined gel can endure and generate great forces. Thus, the force generated by a strong hydrogel actuator becomes

$$F = K A_c \frac{\int_0^t Q_n dt}{V_m}, \quad (2.2)$$

with A_c being the area where the force is applied. Now, we investigate the swelling of polyelectrolyte gels without electric fields to find the net

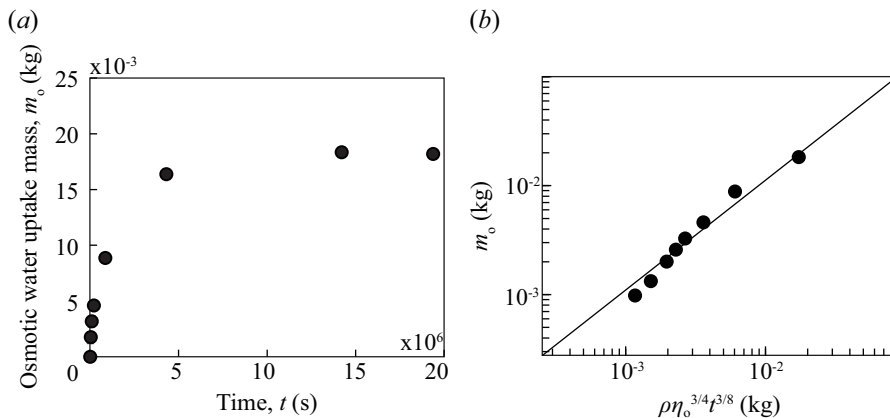


Figure 2.4: (a) Osmotic water uptake mass of gels, m_o over time. (b) Osmotic water uptake mass of gels plotted according to eq. (2.6).

flow rate into the gel to estimate the force generated by a strong hydrogel actuator without electric fields.

When a bare polyelectrolyte hydrogel is submerged in water without an electric field, the gel absorbs the water by osmosis. Osmosis is the diffusion of water across a selectively permeable membrane from a compartment of higher water potential to that of lower water potential. The diffusion process is very slow, so the gel slowly reaches its maximum volume in $\sim 10^7$ sec (see Figure 2.4 (a)). The diffusion flux associated with osmosis, q_o , follows Fick's law

$$q_o = \frac{-Dc\Omega_l\nabla\Psi_s}{RT}, \quad (2.3)$$

with D , c , Ω_l , R , and T respectively being the self-diffusion coefficient of liquid, the liquid concentration of the gel, and molar volume of liquid, gas constant, and temperature (Bird *et al.*, 2006). Here, the difference of the potential of gel for swelling, which we term swelling potential henceforth, Ψ_s is given by $\Delta\Psi_s = \Psi_w - \Psi_o$ where Ψ_w and Ψ_o is the potential of surrounding solution and the osmotic potential of the gel, so that $\Delta\Psi_s = \Pi$ with Π corresponding to the well-known osmotic pressure. Thus, the

2.4 Theoretical analysis

diffusion flow rate is written as

$$Q_o = \frac{Dc\Omega_l\Pi A}{\delta RT}, \quad (2.4)$$

where δ and A are the ion concentration boundary layer thickness that is scaled as \sqrt{Dt} and the surface area of the gel, respectively. Because the volume of bare PSPA gel can expand as much as they absorb water, the variables related to the size of the gel, such as the liquid concentration of the gel c corresponding to V_w/V , the osmotic pressure Π that is ic_dV_dRT/V , and the surface area $A = 6V^{2/3}$. Here, i , c_d , V_d , and V are van't Hoff's factor, the polymer concentration of the dry gel, the volume of the dry gel and the total volume of the swollen gel, respectively. Therefore,

$$Q_o \sim 6ic_dV_d\Omega_l D^{1/2}V_w^{-1/3}t^{-1/2}, \quad (2.5)$$

By taking $Q_o = dV_w/dt$, we get the osmotic water uptake mass of the PSPA gel

$$m_o = \rho\eta_o^{3/4}t^{3/8}, \quad (2.6)$$

where ρ is the density of water and $\eta = i\alpha_o c_d V_d \Omega_l D^{1/2}$ with α_o being the proportional constant. Here, we use the 3 M PSPA gel whose volume at dry state is $5 \times 10^{-7} \text{ m}^3$ and water whose D , Ω_l and ρ are $2.3 \times 10^{-9} \text{ m}^2\text{s}^{-1}$, $1.8 \times 10^{-6} \text{ m}^3\text{mol}^{-1}$, and 997 kgm^{-3} . By taking $i = 2$ and $\alpha_o = 30$, we calculate the osmotic water uptake mass of 3 M PSPA gel and compare it with the measured value as shown in figure 2.4 (b). We see that the calculated osmotic water uptake masses agree well with the experimental data.

In the strong hydrogel actuator, the swelling potential Ψ_s and internal potential developed by osmosis Ψ_m , $\Psi_s = \Psi_o + \Psi_m$, so the diffusion flow rate into the strong hydrogel actuator is written as

$$Q'_o = \frac{Dc\Omega_l(\Psi_o + \Psi_m)A}{\delta RT}. \quad (2.7)$$

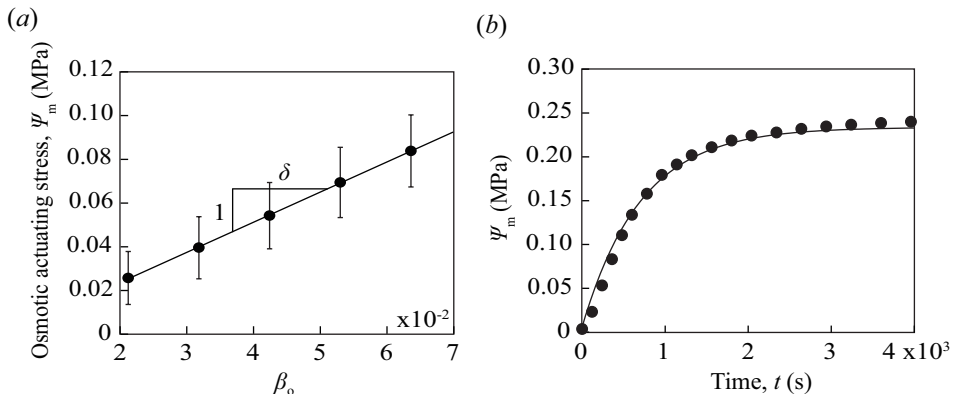


Figure 2.5: (a) Osmotic actuating stress Ψ_m versus $\beta_o = Dc\Omega_l K A \Pi t / (RTV_m)$. The slope of the best-fitting line corresponding to $1/\delta$ is 1.4×10^6 m-1. (b) Osmotic actuating stress over time. The solid lines correspond to the theoretical osmotic actuating stress of the strong hydrogel actuator. The error bar is standard deviation of measurement values.

Here, the osmotic potential induces the diffusion of liquid into the gel, while the internal potential reduces this tendency of liquid. In eq. (2.7), for the strong hydrogel actuator, c and δ are constant owing to the gel's fixed volume by the relatively stiff membrane surrounding the gel. The internal potential corresponds to the internal stress developed inside the gel restrained from swelling, $\Psi_m = K\gamma_h$. Because γ_h is originated from $\int q_o A dt / V_m$, we get $\Psi_m = K \int q_o A dt / V_m$. Substituting $Q'_o = V_0(d\Psi_m/dt)/K$ in eq. (2.7) and solving, we get

$$\Psi_m = \Pi(1 - e^{-t/\tau_o}), \quad (2.8)$$

with $\tau_o = RTV_m\delta / (Dc\Omega_l K A)$.

The strong hydrogel actuator used in this study is composed of a cubic dry gel with a volume of 5×10^{-7} m³ enveloped by a stiff membrane with a thickness of 1.5 mm. This actuator is activated when the space enclosed by the membranes is filled with the swollen gel. Then the activated actuator assumes a cubic shape, with a base area of 4 x 2.3 mm and a height of 8 mm. Therefore, the liquid inlet area A and the volume of the strong

2.4 Theoretical analysis

hydrogel actuator V_m are approximately $1.6 \times 10^{-3} \text{ m}^2$ and $3.2 \times 10^{-6} \text{ m}^3$, respectively. For the actuator, which exerts force to the exterior at the gel swelling ratio of 6.3 and sustains its volume during the actuation, the liquid concentration in the gel c and the empirically predicted osmotic pressure Π are maintained as 0.9 and 0.27 MPa, respectively. The water distribution inside the constrained gel is approximately uniform except within the boundary layer at the interface between the gel and the membrane. The potential gradient is established in this boundary layer with the thickness of δ . In the early stages of actuation, where the decrease in swelling potential due to the internal potential is negligible, the internal potential developed by osmosis is generated just by osmotic potential. Thus, $\Psi_m = \beta_o/\delta$ with $\beta_o = Dc\Omega_l K A \Pi t / (RTV_m)$. Here, the internal potential developed by swelling appears as actuating stress of the strong hydrogel actuator without an electric field. By plotting the actuating stress without an electric field in the early stages versus β_o in figure 2.5(a), we obtain $\delta = 700 \text{ nm}$. Using these parameter values, we calculate the theoretical osmotic actuating stress of the strong hydrogel actuator and plot the result as solid lines in figure 2.5(b). We see that the calculated actuating stress agrees well with the experimental data.

2.4.2 Stress generation dynamics in electric fields

When a polyelectrolyte gel having sulfur functional groups is wet, the functional groups of polymer chains dissociate into ions, so the polymer chains are charged, and the liquid in the gel becomes an electrolyte solution. Here, the electric fields can act as a stimulus affecting the swelling process of the polyelectrolyte gel. As shown in figure 2.6 (a), we measure the mass of the PSPA gel over time with electric fields ranging from 0 to 600 V m^{-1} , and find that the electric fields remarkably accelerates the water uptake rate of the polyelectrolyte gel. The PSPA gel absorbs the water proportional to the time when the electric fields are applied, and the electroosmotic water

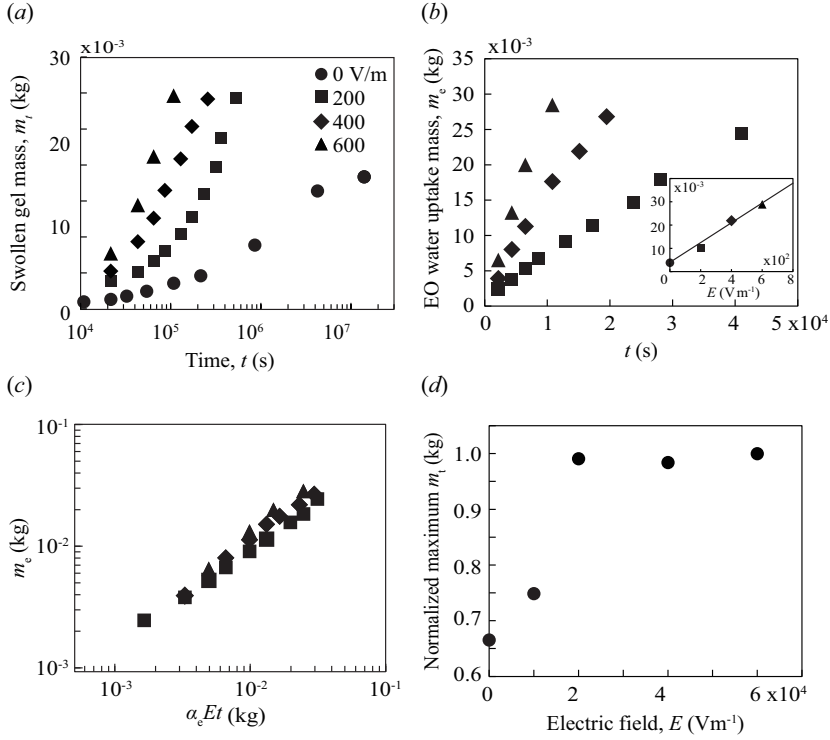


Figure 2.6: (a) The mass of swollen gels m_t in electric fields from $E = 0$ to 600 V m^{-1} . (b) Electroosmotic(EO) water uptake mass of gels m_e over time in electric fields ranging from 200 to 400 V m^{-1} . Inset: Electroosmotic(EO) water uptake mass of gels m_e in electric fields from 0 to 400 V m^{-1} at $t = 2000 \text{ s}$. (c) EO water uptake mass of hydrogels, plotting according to $\alpha_e Et$, where $\alpha_e = \rho \epsilon \zeta \phi A / \mu$. (d) The normalized maximum mass of swollen gels m_n according to electric fields from 0 to 600 V m^{-1} . The normalized maximum mass of swollen gel is obtained by dividing the maximum mass of a swollen gel at each electric fields to the maximum mass of a swollen gel in 600 V m^{-1} .

2.4 Theoretical analysis

uptake mass of the polyelectrolyte gel at the same time is proportional to the strength of electric fields (see Figure 2.6 (b)).

Polyelectrolyte gels are generally considered as the charged porous media that the pores are filled with electrolyte solution having an ionic layer known as an electric double layer at the interface between the wall and the liquid. When the electric fields are applied on this polyelectrolyte gel, the net charge of the electric double layer moves by electric fields while dragging liquid. Here, the induced liquid flow is called electroosmotic (EO) flow. Thus, under an electric field, polyelectrolyte gels can absorb the water by both osmosis and electroosmosis. The polyelectrolyte gel composing contains 3.0 M PSPA, whose dissociation degree is approximately 1. Thus, the wet gel can be modeled as a porous medium filled with the electrolyte solution with the molarity c_g of 3.0 M. In an electrolyte solution, the Debye length λ_d is calculated as

$$\lambda_d = \left(\frac{\epsilon k_B T}{2(z e)^2 c_g} \right)^{1/2}, \quad (2.9)$$

where e , z , k_B , and ϵ are respectively the elementary charge, valence of the ions ($z = 1$, in our case), the Boltzmann constant, and permittivity. For 3 M ionic solution, we estimate a Debye length of $\lambda_d \approx 0.2$ nm and therefore λ_d is much smaller than the average pore size of the gel $r \sim 10$ nm (Chan & Neufeld, 2009; Cuccia *et al.*, 2020; Varghese *et al.*, 2014). Then, the electroosmotic flux is given as

$$q_e = \frac{\epsilon \zeta \phi E}{\mu}, \quad (2.10)$$

with ϕ , ζ and μ being the porosity of the gel, the zeta potential at the pore wall and viscosity of liquids, respectively (Probstein, 2005), so the electroosmotic water uptake mass

$$m_e = \alpha_e E t, \quad (2.11)$$

2.4 Theoretical analysis

with $\alpha_e = \rho\epsilon\zeta\phi A/\mu$. The PSPA gel in electric fields absorbs the liquid by both osmosis and electroosmosis, thus the total liquid influx to the hydrogel in electric fields $q_t = q_o + q_e$. It leads the total water uptake mass of the gel to

$$m_t = \alpha_e Et + m_o. \quad (2.12)$$

Here, the liquid properties ϵ and μ of water which is $7.08 \times 10^{-10} \text{ F m}^{-1}$ and $10^{-3} \text{ Pa}\cdot\text{s}$, respectively. The zeta potential of PSPA gel is $\zeta = -80 \text{ mV}$ (Daniel *et al.*, 2021). We take the average porosity of the gel during the swelling $\phi \approx 0.5$. Using these values, we calculate the theoretical electroosmotic water uptake mass of the gel under the electric fields ranging from 0 to 600 V m^{-1} and compared the result to the experimental data in figure 2.6(c). We see that the calculated EO water uptake mass agrees well with the experimental data.

Furthermore, the electric fields affect the maximum mass that a gel can achieve. As depicted in figure 2.6(d), the normalized maximum mass of the gels m_n in electric fields is much larger than that without electric fields. Here, m_n in electric fields over 100 V m^{-1} are very similar to each other. The maximum mass of the gels is determined by the physical stretch limit of polymer chain x , and this stretch limit can be elongated by external forces f .

The polymer chain length determines the swelling limit of the gel, and external forces applied on a polymer chain f elongates the polymer chain length x . As the applied force increases, the polymer chain length elongates up to its stretch limit x_c , which is the physically possible maximum polymer chain length. For a freely jointed chain, the normalized polymer chain length x/x_c follows the Langevin function with the normalized extensional force $fb/k_B T$, leading to

$$\frac{x}{x_c} = \coth\left(\frac{fb}{k_B T}\right) - \left(\frac{fb}{k_B T}\right)^{-1}, \quad (2.13)$$

2.4 Theoretical analysis

where b , k_B , and T being the Kuhn length, Boltzmann constant and temperature (Rubinstein *et al.*, 2003). According to eq. 2.13, the polymer chain length reaches 95% of the stretch limit when the normalized extension force is 20. The force exerted on a polymer chain by the applied electric field corresponds to the drag force induced by electroosmotic flow. The hydraulic drag force F_d on a pore comes from the shear stress τ on a pore wall, so $F_d = \tau A_p$ with A_p being the surface area of the pore wall. The shear stress τ is $\mu U/r$ where the liquid velocity U is electroosmotic flow velocity written as $\epsilon E \zeta / \mu$, and r is the pore size. By applying $A_p = 2\pi r L$ with L being the length of hydrogel, we get $F_d = 2\pi \epsilon E \zeta L$. For the electric field $E \sim 1$ V, the normalized extension force becomes 20, so the polymer chain length elongation is saturated over $E \sim 1$ V which matches closely to the measurement depicted in figure 2.6(d).

Since the polyelectrolyte gels can absorb the water by both osmosis and electroosmosis under an electric field, the swelling potential Ψ_s consists of osmotic swelling potential $\Psi_{s,o}$ and electroosmotic swelling potential $\Psi_{s,e}$. Unlike the osmotic swelling potential, the electroosmotic swelling potential $\Psi_{s,e}$ is determined by electroosmotic potential Ψ_e and internal potential developed by electroosmosis Ψ_p . Here, the electroosmotic potential drives the liquid flow into the gel, whereas the internal potential tends to drive the liquid flow out of the gel. The flow driven by the internal potential follows Darcy's law,

$$q_p = -\frac{k}{\mu} \nabla \Psi_p, \quad (2.14)$$

which describes the viscous liquid flux q_p through a porous medium with the permeability k . Thus, the total inlet flow rate is the difference between the electroosmotic influx and the internal stress-driven outflux:

$$Q'_e = \frac{\epsilon \zeta E \phi A L - k A \Psi_p}{\mu L}, \quad (2.15)$$

where L is the characteristic length of the polyelectrolyte gel. Here, L is the average half-length of the gel, 16 mm. Q'_e causes the internal potential

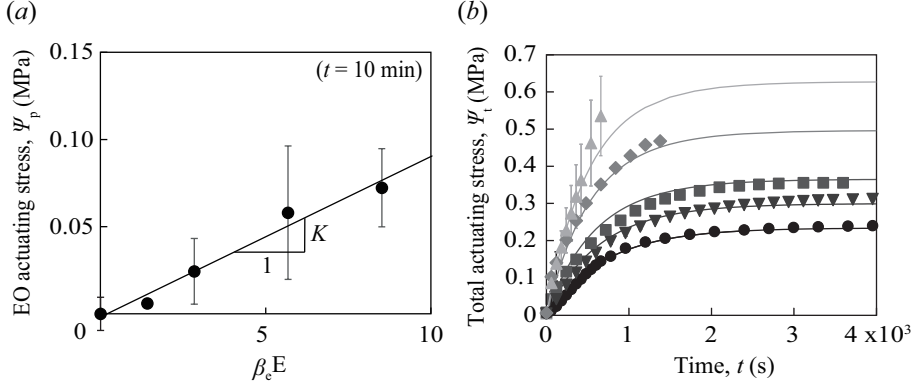


Figure 2.7: (a) Electroosmotic (EO) actuating stress Ψ_p versus $\beta_e E$, where $\beta_e = \epsilon\zeta E\phi At/(V_m\mu)$ and $t = 10$ min. The slope of the best-fitting line corresponding to K is 9.2 kPa. (b) The total stress generated by strong hydrogel actuator over time in different electric fields such as 0 (circle), 100 (inverted triangle), 200 (square), 400 (diamond), and 600 V m^{-1} (triangle).

as a result of a volumetric strain $\Psi_p = K \int Q'_e dt/V_m$. Substituting $Q'_e = V_m(d\Psi_p/dt)/K$ in this equation, we get

$$\Psi_p = \eta_e(1 - e^{-t/\tau_e}), \quad (2.16)$$

with $\eta_e = \epsilon\zeta E\phi L/k$ and $\tau_e = \mu LV_m/(kKA)$. Therefore, the total internal potential $\Psi_t = \Psi_p + \Psi_m$, is obtained as

$$\Psi_t = \Pi(1 - e^{-t/\tau_o}) + \eta_e(1 - e^{-t/\tau_e}). \quad (2.17)$$

In the early stages of actuation, where the decrease in swelling potential due to the internal potential is negligible, the internal potential developed by electroosmosis is determined just by electroosmosis. Thus, $\Psi_p = K\beta_e E$ with $\beta_e = \epsilon\zeta E\phi At/(V_m\mu)$. Here, the internal potential developed by electroosmosis appears as actuating stress of the actuator with electric fields. By plotting the actuating stress with electric fields at $t = 10$ min versus $\beta_e E$ in figure 2.7(a), we obtain the bulk modulus of the gel $K = 9.2$ kPa from the slope of the best-fitting line. The permeability of polyelectrolyte gel k is

2.4 Theoretical analysis

scaled as the fluid conduit area, so that we write $k = \alpha r^2$ with α being the proportionality constant. In our theoretical calculation for the electroosmotic actuating stress of the strong hydrogel actuators, the proportionality constant α is found to be 14. Using the parameter values obtained from literature and experiments, we calculate the total actuating force of the strong hydrogel actuator and plot the result as solid lines with the same color as the experimental data in figure 2.7(b). We see that the calculated total actuating forces agree well with the experimental data under electric fields ranging from 0 to 600 V m⁻¹.

2.4.3 Maximum stress

Based on eq. 2.17, we predict the maximum stress generated by a strong hydrogel actuator as follows:

$$\sigma_{max} = \frac{ic_dRTV_d}{V_m} + \frac{\epsilon\zeta E\phi L}{k}. \quad (2.18)$$

Here, the porosity states the volume fraction of the non-polymeric part in the swollen gel, $\phi = 1 - V_d/V_m$, and the characteristic length L correspond to the average half-length of the gel, so $L \approx 0.5V_m^{1/3}$. Substituting these into eq. 2.18, we obtain

$$\sigma_{max} = \frac{ic_dRTV_d}{V_m} + \frac{\epsilon\zeta E(V_m - V_d)}{2kV_m^{2/3}} \quad (2.19)$$

Consequently, main design parameters of the strong hydrogel actuator controlling the maximum stress are the volume of the dry gel V_d and the size of a membrane that determines the maximum volume of the membrane can wrap V_m . By taking $\chi = V_m/V_d$, we get the maximum stress of a strong hydrogel actuator without an electric field

$$\sigma_{max,o} = \frac{ic_dRT}{\chi}, \quad (2.20)$$

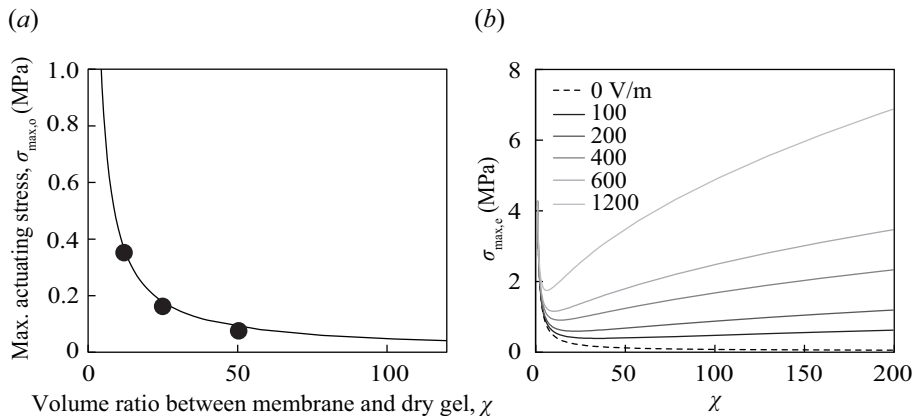


Figure 2.8: (a) The maximum stress generated by the strong hydrogel actuator without electric field $\sigma_{max,o}$ according to the ratio of the maximum volume of the membrane can envelop to the dry gel volume χ . (b) The maximum stress generated by the strong hydrogel actuator with electric fields ranging from 0 to 1200 V m^{-1} according to χ .

and plot the σ_{max} in figure 2.8(a). The larger the membrane size, the smaller the maximum stress generated by the strong hydrogel actuator without an electric field, which implies that the strong hydrogel actuator cannot economically generate great forces. However, the maximum stress generated by a strong hydrogel actuator in electric fields,

$$\sigma_{max,e} = \frac{ic_dRT}{\chi} + \frac{\epsilon\zeta EV_d^{1/3}(\chi - 1)}{2k\chi^{2/3}}. \quad (2.21)$$

Assuming that V_d is constant, $\sigma_{max,e}$ is plotted in figure 2.8(b) according to the strength of electric fields ranging from 0 to 1200 V m^{-1} . In this strong hydrogel actuator in electric fields, even the membrane size becomes larger, the maximum stress generated by the strong hydrogel actuator is consistent or even increases. Based on these findings, we find that the electric fields would help the strong hydrogel actuator to generated great forces economically.

2.5 Conclusion

With a simple and novel strategy, we have fabricated the hydrogel actuator, termed as a strong hydrogel actuator, having high strength and durability against compression and also propose a way to accelerate the response time of the hydrogel actuator. With the fundamental understanding of the swelling of polyelectrolyte gel within and without electric fields, we have theoretically and experimentally studied the force generation dynamics of strong hydrogel actuators and predicted the maximum stress of those according to electric fields. Based on our findings, we have derived the main design parameters of the strong hydrogel actuator.

This system has the strengths of providing great force in the water and high resistance to deformation. Thus, the system is applicable for the construction of heavy buildings underwater (for example, posts in bridges or support beams in submarine tunnels), which always accompany difficult and complex processes and fabrication of soft robots or actuators requiring large force or stiffness. The strong hydrogel system simultaneously solves the chronic problems of hydrogel: the lack of mechanical properties, susceptibility to deformation, and low response rate. Besides, the strategy to fabricate the strong hydrogel system is easy and universally applicable to any soft polymer network, so we expect this system to open up a new era of application for these kinds of materials.

Chapter 3

Dissolution dynamics: Dynamics of soluble wicking

3.1 Introduction

Liquid flows infiltrating into porous media are found in a variety of situations, including painting (Kim *et al.*, 2015) and writing (Kim *et al.*, 2011) on paper, wetting of soils (Raux *et al.*, 2013) and hydrogels (Yoon *et al.*, 2010), and absorption in hygiene items (Landeryou *et al.*, 2005). When the media are wettable but insoluble in the liquid, the flow velocity is determined by the balance of capillary driving force and viscous resisting force. A simple approach considering the voids an assemblage of cylindrical conduits predicts that the wetting distance will grow like $t^{1/2}$ with t being time (Washburn, 1921), which has been widely adopted to explain basic wetting dynamics of porous media over a century. However, variations of the wetting dynamics can arise for a number of factors, such as effects of gravity (Kim *et al.*, 2017), poroelastic response of soft solids (Ha *et al.*,

The contents of this chapter were published as (Jung *et al.*, 2020) and (Jung *et al.*, 2021) papers.

2018), spatial irregularities or directionality of pore networks (Xia *et al.*, 2013), and solubility of medium solids (Twist & Zatz, 1988).

Liquid invasion in soluble porous media plays an essential role in geological sequestration (Geller & Hunt, 1993) and exploration (Chao, 1984), microfluidics (Jahanshahi-Anbuhi *et al.*, 2013), and drug delivery (Lopes *et al.*, 2016; Sujja-areevath *et al.*, 1998). In geological application, liquid flows caused by pressurized injection, rather than spontaneous capillary imbibition, and subsequent dissolution in soluble porous media were previously investigated with a major focus on the formation of ramified patterns (Daccord, 1987; Szymczak & Ladd, 2011). In drug delivery, the role of porosity in drug release rate was experimentally studied when the governing step of drug response was swelling (Colombo *et al.*, 1996) or dissolution (Brielles *et al.*, 2007). Despite these pioneering but limited studies, the fundamental physical understanding of capillarity-driven imbibition dynamics coupled with dissolution has rarely been attempted and as a result is still far from complete.

Here, we study the wicking dynamics in soluble porous polymer having different solubilities. As a model system to study the dynamics of soluble wicking, we use porous sheets of polyethylene oxide (PEO) fibers. PEO can be dissolved into water and chloroform but is insoluble in ethylene glycol and silicone oil. Also, the solubility of PEO is differed depending on the concentration of its constituents in aqueous solutions. According to the polymer's solubility, we classified the soluble flows into partially soluble and completely soluble wickings. We then theoretically analyze each soluble wickings where the fundamental wicking dynamics in insoluble porous sheets of randomly deposited fibers serve as a basis to identify the effects of polymer solubility on the rate of wicking dynamics. In partially soluble flow, we find that imbibition with dissolution is markedly slower than without dissolution, but the rate of wicking is determined by the same dynamics of the insoluble wicking, which is the balance of capillary driving force and viscous resistance. We develop a mathematical model to predict

3.2 Classification of soluble wicking regime

the rate of wicking, which explains how dissolution changes the viscosity of the invading liquid and affects the wicking dynamics. In completely soluble flow, we find that the wicking rate is determined by a completely different process from the insoluble wicking, thereby giving different power laws of wicking distance. With observations of porous polymers during and after completely soluble wicking by microscopy and scanning electron microscope (SEM), we discover the formation of a gel layer that strongly inhibits the wicking by clogging the pores. The wicking can reappears after this gel layer is removed by dissolution. We also find that the durability of a gel layer is determined by the microstructure of porous polymers. Based on these findings, we propose the strategy to control the direction of soluble wicking with controlling the structure of the porous medium and show its possibility with a porous sheet composed of aligned PEO nanofibers exhibiting dramatic directional soluble wicking.

3.2 Classification of soluble wicking regime

As a model system to study the dynamics of soluble wicking where liquids infiltrates into porous polymer substrates, we used sheets of fibers of PEO (Sigma Aldrich) with the molecular weight of 3×10^5 , which were produced by electrospinning. A jet of aqueous PEO solution of 10 wt% concentration was ejected from a metal capillary 0.26 mm in inner diameter under an electric field of 100 kV m^{-1} . The jet was partially solidified during flight and deposited on a flat plate collector as fibers. The fibers were chaotically deposited as shown in figure 3.1 to yield a sheet of the average thickness of $77 \text{ }\mu\text{m}$. The average radius of fibers was measured using SEM (scanning electron microscopy) images, and the porosity was obtained by comparing the densities of PEO and the fibrous sheets. The characteristics of the fibrous sheets are listed in table 3.1.

The liquids used in our experiments are ethylene glycol, silicone oil, water, aqueous ethylene glycol of various concentrations, and chloroform,

3.2 Classification of soluble wicking regime

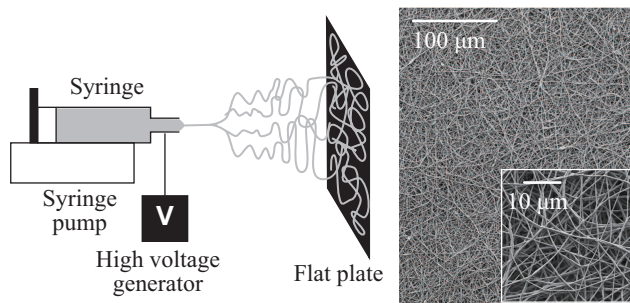


Figure 3.1: A schematic diagram of random deposition of electrospun fibers of PEO to produce a fibrous polymer sheet, and the corresponding SEM image of the sheet.

Fiber radius, R_f , \pm std (nm)	209 ± 38
Porosity, ϕ	0.84
Equivalent pore radius, R (μm)	2.3
Permeability, k , measured (m^2)	4.8×10^{-14}
Permeability, k , modeled (m^2)	4.8×10^{-14}

Table 3.1: Characteristics of the porous fibrous sheets. In fiber radius, std stands for standard deviation.

3.2 Classification of soluble wicking regime

	Liquids	Surface tension (mN m ⁻¹)	Viscosity (mPa·s)	Density (kg m ⁻³)	Symbol
A	Ethylene glycol (EG)	49	21.1	1112	●
B	Silicone oil	40	10.0	939	◆
C	Aqueous EG 70 wt%	53	8.4	1078	■
D	Aqueous EG 20 wt%	59	1.9	1068	◀
E	Aqueous EG 10 wt%	67	1.4	1042	▶
F	Water	72	1.0	997	▲
G	Chloroform	27	0.6	1490	▼

Figure 3.2: Properties of liquids used in the experiments at a temperature of 25°C. Symbols are also listed that appear in figures 3.5 and 3.9 indicating the experimental condition.

whose physical properties are listed in table 3.2. Liquids A and B have a contact angle of nearly zero with PEO sheets but do not dissolve the fibers, while liquids C partially dissolves the fibers with an almost zero contact angle. The other liquids (D to G) dissolve PEO. Here, liquids C to E is the mixture of solvent (water) and non-solvent (ethylene glycol) in PEO, so PEO has different solubility towards these liquids. We evaluated liquid C to E's capacity to dissolve PEO, which is related to the solubility, by measuring the time taken for a complete dissolution of the PEO sheet measuring 10 mm × 2 mm. The dissolution time was on the order of 10 s up to an EG concentration of 60 wt%. This dissolution time is exhibited a sharp rise at an EG concentration higher than approximately 70 wt% so that a complete dissolution was not observed in a week (see Figure 3.3).

During the soluble wicking test, the tip of a 1 cm wide strip of fibrous PEO sheet is dipped into the free surface of a liquid pool, as shown in figure 3.4(a). We observed the imbibition of aqueous EG solutions through a porous PEO sheet. When a PEO sheet was brought into contact with a reservoir, it absorbed the aqueous EG solution. The motion of the imbi-

3.2 Classification of soluble wicking regime

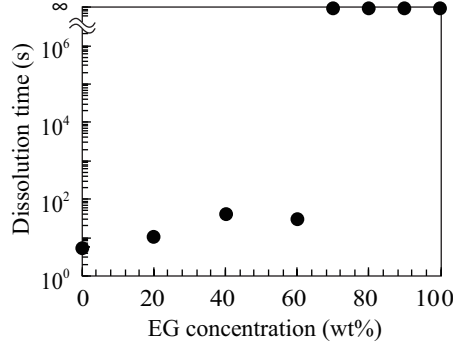


Figure 3.3: The dissolution rate of the porous PEO sheet according to the EG concentration. In the completely soluble wicking regime, PEO dissolves in the order of 10 s. In the partial soluble wicking regime, PEO does not fully dissolve even a week after.

bition front was recorded using a video camera (HDR-CX900, Sony) (Fig. ??a) and the average imbibition height was assessed by measuring the wet area and dividing it by the width of the PEO sheet. The relative humidity and temperature were maintained at $\sim 20\%$ and 25°C , respectively. Here, we classify the soluble wicking regimes into two parts based on the retention of fibrous PEO sheets, which is related to the liquids' capacity to dissolve PEO, during the soluble wicking. One wicking regime is that the wicking of liquids having low capacity to dissolve PEO (EG concentration over 70 wt%) where porous PEO sheets do not entirely collapse and keeps their connection to the reservoir during the wicking test. This wicking is named partially soluble wicking. The other wicking regimes is that the wicking of liquids having high capacity to dissolve PEO (EG concentration from 0 to 60 wt%) where porous PEO sheets entirely collapse and lose their connection to the reservoir due to the PEO's enough solubility in the liquids (see Figure 3.4(b,c)). This wicking is called completely soluble wicking. In the following, we analyze each soluble wicking separately.

3.2 Classification of soluble wicking regime

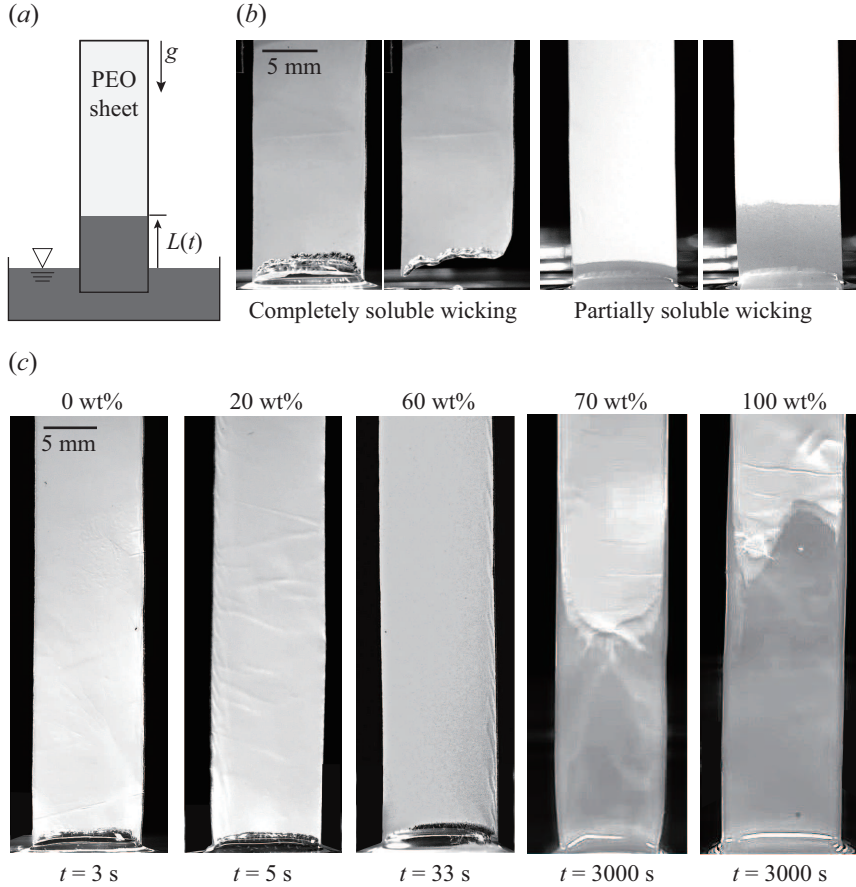


Figure 3.4: (a) Propagation of liquid front against gravity into a strip of fibrous PEO. (b) Optical image of the completely soluble wicking and partially soluble wicking in fibrous PEO sheets. In the completely soluble wicking, a liquid quickly and largely dissolves a fibrous PEO sheet, so the connection between them disappears soon. However, in the partially soluble wicking, a liquid slightly dissolves a fibrous PEO sheet, then the connection between them remains even after a week. (c) Optical image of capillary imbibition of aqueous EG mixtures with various concentrations. In the image of concentrations of 0 to 60 wt%, t denotes the time taking until the sheet departs from the reservoir. In the image of concentrations 70 wt% and pure EG, t denotes the time we took the image.

3.3 Partially soluble wicking

We start with the dynamics of wicking of liquids in insoluble fibrous sheets, whose representative images are shown in figure 3.4(c). As delineated in the introduction of this thesis, in the porous media with homogeneous porosity, one-dimensional fluid flows follow Darcy's law: $q = k\Delta p/(\mu L_p)$, where q , k , and L_p are, respectively, the average fluid velocity over the unit area, the permeability, and the wicking distance. However, the flow velocity that we observe is the average local fluid flow velocity u , which must be greater than the average fluid velocity over the unit area owing to the solid area in porous media. According to the commonly accepted hypothesis known as the Dupuit-Forchheimer assumption (Dupuit, 1863; Forchheimer, 1986), the average local fluid flow velocity u is q/ϕ , which leads to $u = k\Delta p/(\phi\mu L_p)$. If capillarity drives the flow in the wettable media with negligible gravitational effects owing to a very low Bond number, $\text{Bo} = \rho g R^2/\sigma \sim O(10^{-6})$, the pressure difference established between the reservoir and the interior of advancing meniscus is equal to the Laplace pressure, $\Delta p = 2\sigma/R$, where R , ρ , and g are the equivalent pore radius, liquid density, and gravitational acceleration, respectively. Modelling the porous sheet structure as the regular array of cylindrical conduits with the equivalent hydraulic radius R , we estimate R using two measurable parameters, porosity ϕ and fiber radius R_f , as $R = R_f\phi/(1 - \phi)$ (Mao & Russell, 2008). Then, taking $u = \dot{L}_p$ in Darcy's law and integrating with respect to time from $t = 0$ to t gives

$$L_p = 2 \left[\frac{(1 - \phi)k \sigma}{\phi^2 R_f \mu} \right]^{1/2} t^{1/2}. \quad (3.1)$$

This equation suggests that liquid infiltration through a porous medium exhibits diffusive behavior with a diffusion coefficient of

$$D_c = \left[\frac{4(1 - \phi)k \sigma}{\phi^2 R_f \mu} \right]^{1/2} \quad (3.2)$$

(Washburn, 1921).

3.3.1 Experimental analysis

Figure 3.4(c) shows PEO sheets that absorb an aqueous EG mixture from the bottom. The liquid with a concentration of less than 60 wt% has the significant capacity to dissolve PEO, so that the PEO sheet was detached from the reservoir as its bottom was dissolved away. For the cases of aqueous EG mixtures with a concentration greater than 70 wt%, the PEO sheets maintained contact with the liquid reservoir and absorbed the liquid to a significant height. Figure 3.5 shows the dependence of the imbibition length L_p on time t for EG mixtures with a concentration of 70 wt% and pure EG. The plots for both concentrations show the diffusive behavior, $L_p \sim t^{1/2}$. We note that the imbibition velocity of the 70 wt% EG mixture is approximately 0.7 times slower than that of the pure EG. Two liquids have comparable surface tensions, but have significantly different viscosities (see Table 3.2). With the consideration of the capillary diffusivity $D_c \sim (\sigma/\mu)^{1/2}$, one can expect the flow velocity ratio of 70 wt% EG mixture to pure EG to be $u_{70}/u_{100} \sim (\sigma_{70}/\sigma_{100})^{1/2}(\mu_{70}/\mu_{100})^{-1/2} \sim 1.7$, where the subscripts represent the EG concentration. However, our experimental results show a lower imbibition velocity for the 70 wt% EG mixture.

3.3.2 Theoretical analysis

To rationalize our experimental observations, we develop a mathematical model for liquid imbibition through a partially soluble porous medium by considering its dissolution. One may conjecture that PEO fibers swell during the dissolution, thus resulting in a change of the permeability. To evaluate the swelling ratio of PEO fibers in 70 wt% EG mixture, we visualized the microstructure of the PEO sheet before and after wetting using a scanning electron microscope (SEM) (SIGMA, Carl Zeiss) and environmental scanning electron microscope (ESEM) (XL-30 FEG, Philips) (see Figure 3.6(a)). For the visualization with ESEM, we prepared a PEO sheet

3.3 Partially soluble wicking

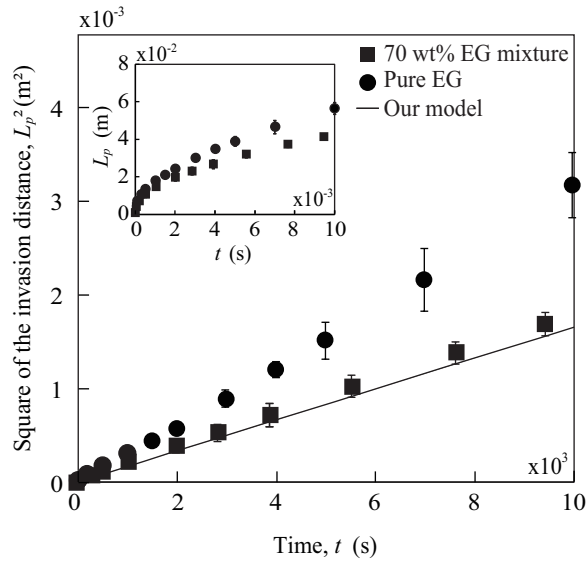


Figure 3.5: The time dependence of the square of the liquid invasion distance (L_p^2) of 70 wt% EG mixture and pure EG. The solid line indicates our model prediction. Inset: a plot with the vertical axis representing the invasion distance L_p .

3.3 Partially soluble wicking

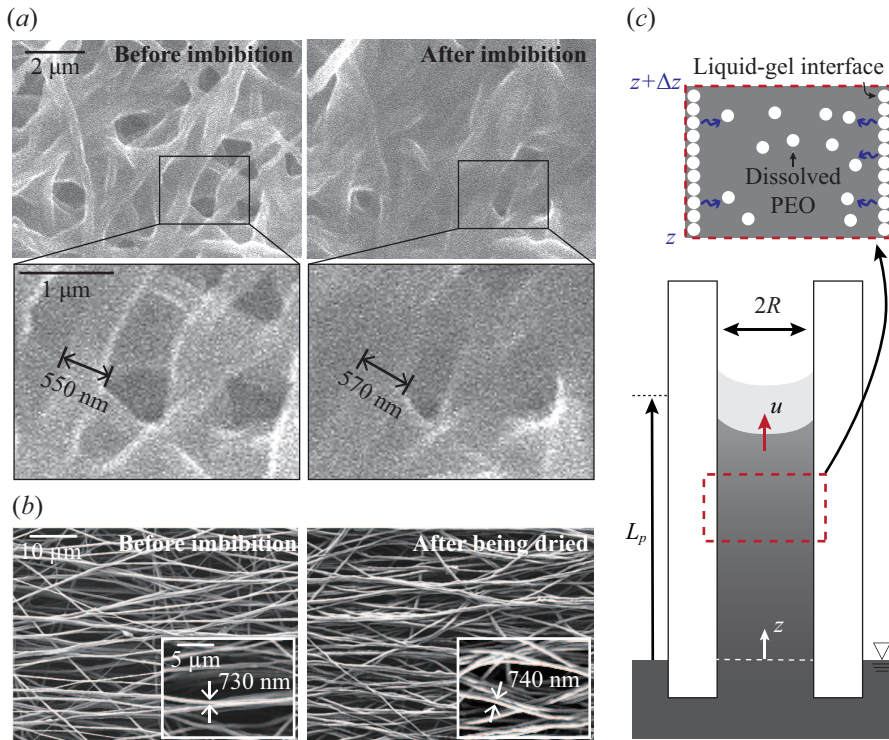


Figure 3.6: (a) The environmental scanning electron microscope (ESEM, Philips XL-30 FEG) images of a PEO sheet before and after it imbibes 70 wt% EG mixture. The polymer fiber swells, and the fiber thickness becomes $1.2 (\pm 0.37)$ times greater than the initial value. (b) SEM images of the PEO sheet. The left image shows an initial PEO sheet, and the right shows a dehydrated PEO sheet after imbibing 70 wt% EG mixture. (c) Schematic illustration of liquid absorption through a tube with the radius R made of soluble material. The red dotted box represents the control volume for analyzing the dissolved PEO mass.

3.3 Partially soluble wicking

composed of nanofibers with a size of $5 \text{ mm} \times 5 \text{ mm}$ on a Peltier plate and put a 70 wt% EG mixture droplet at the edge of the PEO sheet. To suppress condensation for clear visualization, the surface temperature of the Peltier plate and the relative humidity of the ESEM chamber were kept at 2°C and 25%, respectively. From the measurement of the fiber diameter before and after liquid absorption, we found that the swelling ratio is approximately $1.2 (\pm 0.37)$. In figure 3.6(b), no discernable degradation of fiber was observed after being dried again. We estimate that the change in the fiber diameter is on the order of 100 nm, which is much smaller than the pore size $R \sim 2.3 \text{ }\mu\text{m}$. Hence, we assume that the swelling of PEO fibers exerts negligible effects on the permeability. Besides, we observed only little structural deformation of the wet PEO sheet, leading to the assumption that the pore structure remains unchanged during liquid absorption.

The dissolution and swelling of PEO can alter the surface tension and viscosity of the invading liquid, thus possibly resulting in a change in the capillary diffusivity D_c . We measured the dependence of the surface tension of 70 wt% aqueous EG mixtures on the PEO concentration. Surface tension was measured using a force tensiometer (K-100, KRUSS) and hardly depends on the PEO concentration, as shown in figure 3.7(a). In addition, water absorption of PEO fiber negligibly changes the ethylene glycol concentration of the mixture, and we therefore exclude the effects of the surface tension change including the Marangoni effect (Zhang *et al.*, 2018a). We also measured the dependence of the zero-shear viscosity of 70 wt% aqueous EG mixtures on the PEO concentration. To measure the viscosity of EG mixtures, we used a stress-controlled type rheometer with a 60 mm diameter plate (AR-G2, TA Instruments). The measurement was performed in a quasi-steady state at 25°C for 300 s after pre-shearing at 500 s^{-1} during a period of 90 s. The PEO solutions in 70 wt% aqueous EG mixtures exhibited Newtonian behavior over the range of shear rate of $1 - 100 \text{ s}^{-1}$ and PEO concentration of $1 - 38 \text{ gl}^{-1}$, so that the viscosity at a shear rate of 1 s^{-1} was taken as the zero shear viscosity (see Figure 3.7(b)). The zero-shear

3.3 Partially soluble wicking

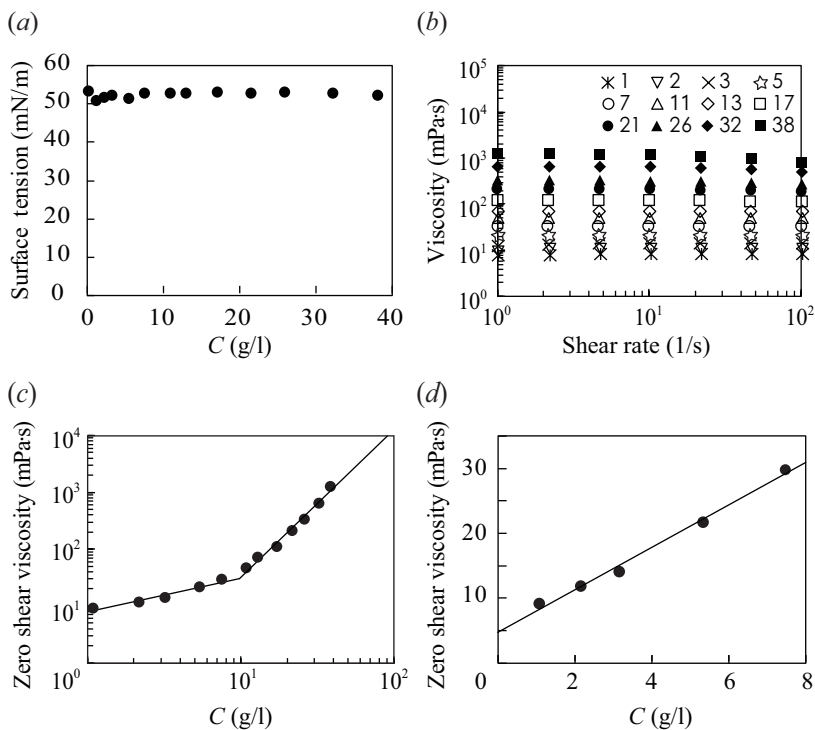


Figure 3.7: (a) The surface tension of 70 wt% EG mixtures versus PEO concentration (C) from 1 to 38 g L^{-1} . (b) Steady shear viscosity of 70 wt% EG mixture at a shear rate ranging from 1 to 100 s^{-1} and various PEO concentrations from 1 to 38 g L^{-1} . Symbols denote PEO concentration in g L^{-1} . (c) Dependence of the zero shear viscosity of 70 wt% EG mixture on. (d) An enlarged plot of the data for PEO concentration between 1 and 7 g L^{-1} .

3.3 Partially soluble wicking

viscosity μ_z increased with the PEO concentrations C . As shown in figure 3.7(c), the dependence of the zero shear viscosity on C sharply changed at a PEO concentration of approximately 10 g L^{-1} , referred to as saturated concentration, at which the phase is known to change from liquid to gel Olatunji (2015). The saturated viscosity of 70 wt% EG mixture, referred to as the viscosity at the saturated concentration, was measured to be $45 \text{ mPa}\cdot\text{s}$ (see Figure 3.7(c)). Our measurement of the viscosity of 70 wt% EG mixture suggests that the viscosity is crucially influenced by the dissolved PEO in the liquid (see Figure 3.7(b)). We consider the viscosity of the invading EG mixture as a varying parameter $\mu = \mu(z, t)$, where z is the length measured from the reservoir.

With the consideration of a variable viscosity, Darcy's law can be written as

$$\frac{dL_p}{dt} = -\frac{k \Delta p}{\mu L_p} \sim \frac{\sigma R}{L_p \mu(z, t)}. \quad (3.3)$$

Solving eq. (3.3) requires the evaluation of the viscosity $\mu(z, t)$, which primarily depends on the PEO concentration. Based on the data shown in the inset of figure 3.7c, we propose a linear dependence of the zero shear viscosity on C for $C < 10 \text{ g L}^{-1}$ in the form of $\mu = \mu_0 + \alpha C$, where μ_0 and α are the viscosity for $C = 0$ and a proportional constant, respectively (see Figure 3.7(d)).

To analyze the local PEO concentration, we idealize the imbibition of aqueous EG mixture through the PEO sheet as liquid absorption through a capillary tube made of soluble material with a radius of R equal to the equivalent pore radius of the PEO sheet. The local solute concentration along the axial direction can be determined by convective and diffusive solute transfer. Given a large Peclet number $\text{Pe} = L_p u / D \sim 100$ in our experiments, where $L_p \sim 10^{-2} \text{ m}$ is the imbibition length, $u \sim 10^{-6} \text{ ms}^{-1}$ is the average flow velocity, and $D \sim 10^{-11} \text{ m}^2\text{s}^{-1}$ is the diffusivity of PEO in water (Waggoner *et al.*, 1995), we neglect the diffusion of PEO in the flow direction. The local PEO concentration is obtained from the mass

3.3 Partially soluble wicking

conservation of PEO in the control volume in figure 3.6(c):

$$\frac{\partial C}{\partial t} = \frac{2h}{R}(C_s - C) - u \frac{\partial C}{\partial z}, \quad (3.4)$$

where h is the convective mass transfer coefficient, and C_s is the saturated PEO concentration. For a fully developed laminar flow, the Sherwood number $Sh = hR/D$ is 3.66 (Thirumaleshwar, 2006), leading to $h \sim D/R$. In our experiments, the ratio of $2h(C_s - C)/R$ to $u\partial C/\partial z$ in the left-hand side is given by $2hL_p/(Ru) \sim 10^5$ with $h \sim 10^{-5} \text{ ms}^{-1}$. Accordingly, the PEO concentration can be assumed to be uniform along the channel, and the solution of eq. (3.4) is given by $C(t) = C_s[1 - \exp(-\beta t)]$ with a constant of $\beta = 2h/R$. By substituting $\mu(z, t)$ in eq. (3.3) with $\mu(t) = \mu_0 + \alpha C_s[1 - \exp(-\beta t)]$, we get

$$L_p dL_p \sim \frac{\sigma R}{\mu_s - (\mu_s - \mu_0) \exp(-\beta t)} dt, \quad (3.5)$$

where $\mu_0 + \alpha C_s$ has been replaced with the saturated viscosity of a solution μ_s , and $\mu_s - \mu_0$ corresponds to αC_s . It can be analytically solved by integrating both sides, and the solution of eq. (3.5) is expressed as

$$L_p \sim \sqrt{\frac{\sigma R^2}{\mu_s h} \ln \left\{ \frac{\mu_s}{\mu_0} [\exp(\beta t) - 1] + 1 \right\}}. \quad (3.6)$$

In the limit of $t > 1 \text{ ms}$, $ht/R \gg 1$, so that $\ln\{\mu_s/\mu_0[\exp(\beta t) - 1] + 1\} \sim \beta t + \ln(\mu_s/\mu_0)$. Since $\ln(\mu_s/\mu_0) \sim 1$ in our experiments, we finally get a simple form of the solution as follows:

$$L_p \sim \left(\frac{\sigma R}{\mu_s} t \right)^{\frac{1}{2}}. \quad (3.7)$$

This solution implies that when the liquid is quickly saturated due to the fast diffusion of the dissolved polymer in the pores, the liquid flow is determined by the saturated viscosity.

To verify our mathematical model, we compare the ratio of the invasion distance of 70 wt% EG mixture to that of the pure EG found in the

3.4 Completely soluble wicking

experimental data, $L_{p,70}/L_{p,100} = 0.75$, with the model prediction, given by $[\sigma_{70}\mu_{s,100}/(\sigma_{100}\mu_{s,70})]^{1/2} = 0.72$, which shows a good agreement. Here $\mu_{s,70}$ is approximately 45 mPa·s (see Figure 3.7(c)). In figure 3.5, the close match between experimental and estimated data (<4%) implies that our mathematical model well explains the unexpectedly slow imbibition of 70 wt% EG mixture.

Besides PEO that we examined, understanding the wicking dynamics of the partially soluble porous polymers can benefit from our theory because polymer having low solubility typically swells little (Brazel & Rosen, 2012; Hildebrand & Scott, 1950; Mah *et al.*, 2018; Navarro-Lupi3n *et al.*, 2005) and does not affect the liquid’s surface tension (Hu *et al.*, 1991; Ishiguro & Hartnett, 1992; Kotchaphakdee & Williams, 1970; Manglik *et al.*, 2001). When the polymer consisting of macromolecules with a molecular size of $1 - 10^3$ nm diffuses into a solvent with a viscosity of $\sim 10^{-3}$ Pa·s, the diffusivity is expected to be $10^{-13} - 10^{-10}$ m²s⁻¹ from the Stokes-Einstein relation (Couper & Stepto, 1969). In this diffusivity regime, the liquid infiltrating the partially soluble polymeric fibrous sheets having sub-micron pores follows eq. (3.7) from the beginning of wicking ($t > 1$ s). Therefore, our theoretical framework can be a useful tool for analyzing liquid infiltration through a wide range of microporous media made of partially soluble polymers.

3.4 Completely soluble wicking

3.4.1 Experimental analysis

While the PEO fibers are partially soluble in liquids C, they are completely soluble in low concentration aqueous solutions (liquids D to F) and chloroform (G). Here, we observed wicking of a liquid emanated from a capillary tube on a porous substrate due to capillary action to check the pattern of the spreading dynamics, as shown in figure 3.8(a). The rate of

3.4 Completely soluble wicking

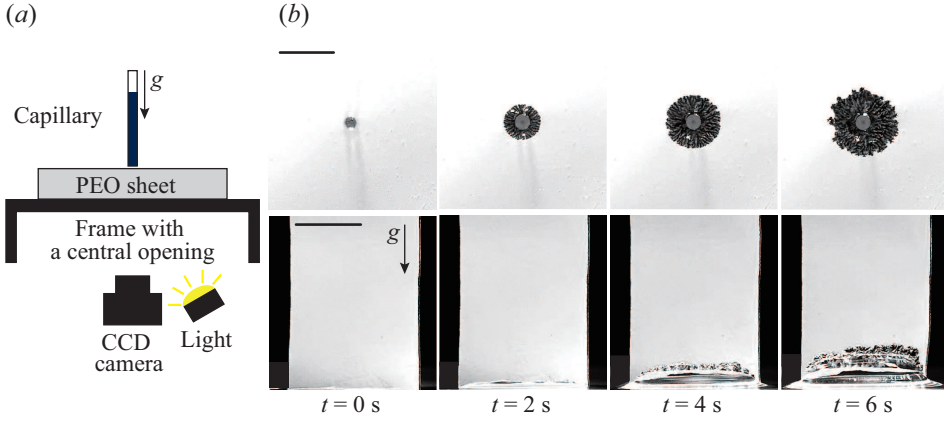


Figure 3.8: (a) Wicking of a liquid from a point source emanating from a capillary tube touching a PEO fibrous sheet. (b) Wicking of water in a randomly deposited soluble sheet. In (b), the up and down rows correspond to the flows from a point sourced (capillary) and a liquid pool, respectively.

one-dimensional wicking was separately measured by observing the propagation of wetting front, $L(t)$, in a 1 cm wide strip from the free surface of a liquid pool, as shown in figure 3.4(a). When liquids touch randomly deposited soluble porous sheets, the wicking tends to occur independent of direction with spiky circular fronts from a point source as shown in the up row of figure 3.8(b). The rough horizontal wetting front advances from a free surface as shown in the down row of figure 3.8(b). Figure 3.9(a–b) shows the soluble wicking dynamics qualitatively different from those in insoluble porous media, i.e. the wicking distance in soluble porous media grows linearly with time rather than increasing like $t^{1/2}$.

3.4.2 Theoretical analysis

The transport of liquid in soluble porous media involves more complex processes than in insoluble porous media. In general, when polymer contacts its solvent, the polymer first swells by absorbing the solvent, and

3.4 Completely soluble wicking

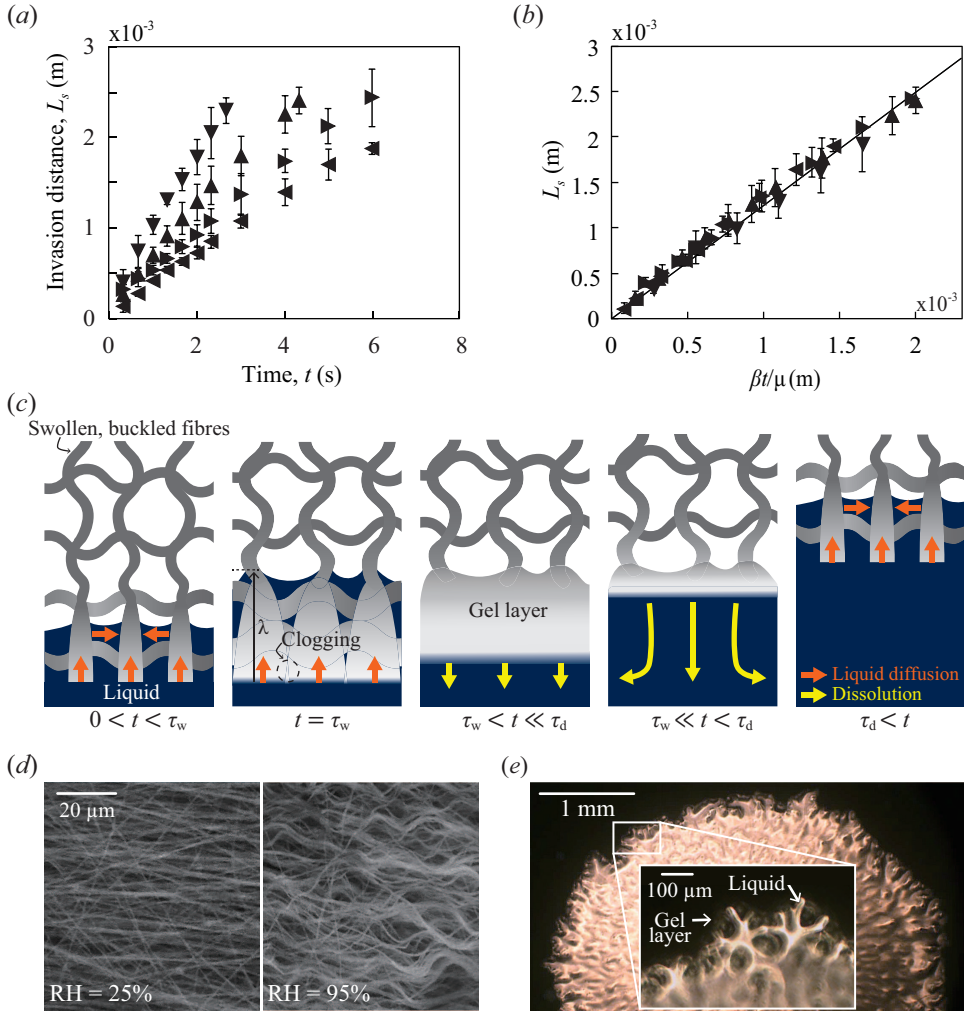


Figure 3.9: (a) The liquid invasion distance, L_s , of various liquids versus time in soluble porous sheets of randomly deposited PEO fibers. (b) L_s versus $\beta t/\mu$, plotted according to scaling law (3.8). (c) Schematics of physical processes during wicking of a porous sheet of randomly deposited soluble fibers. The solvent diffuses in fibers (orange arrows), which swell and turn to gel layer accordingly. The loosened polymer chains are dissolved away (yellow arrows) where they can meet fresh liquid, which becomes an instantaneously preferred direction of soluble wicking. (d) ESEM images of PEO fibers that swell and consequently buckle to contact with their neighbours under a high humidity. (e) Inverted microscopy image of a soluble random porous sheet being impregnated by water, whose wet area appears bright.

3.4 Completely soluble wicking

then turns into gel (a diluted cross-linked system with negligible fluidity). If the gel layer blocks flow paths in the fibrous network, the gel layer should be dissolved away into fresh solvent before liquid propagation resumes. To aid the understanding of soluble wicking dynamics in general, we consider two cases depending on the size of conduit relative to the degree of polymer swelling. First, the conduit is so large that the swelling of polymeric wall does not block the conduit but only modifies the capillary radius and the liquid properties (viscosity and surface tension), as illustrated in figure 3.10(a). Second, the conduit is so narrow that the polymer swelling blocks the channel rapidly as shown in figure 3.10(b). Wicking can resume only when the gel blocking the conduit is dissolved into the solvent.

In the first case, we need to consider simultaneous processes of longitudinal wicking and the polymer wall's transverse diffusion, swelling, and dissolution. That is, as the wall swells, the capillary driving force and the viscous resistance changes for the shrinking cross-section of fluid conduit. We also need to consider the loss of liquid for its transverse diffusion into the polymer wall and possible change of viscosity for polymer dissolution. This is a challenging problem that should couple capillary dynamics, kinetics of solvent diffusion and consequent polymer swelling, and chemical reaction of polymer dissolution into solvent (Ha *et al.*, 2018).

However, the current problem is rather directly linked to the second case of narrow conduits that are readily blocked by swelling polymer fibers. The swelling ratio of PEO due to absorption of aqueous liquids is so high (approximately 10) that voids in our porous sheets with porosity of 0.84 are clogged by the swollen polymer. Then, the wicking arises by repeating the following steps: wall swelling with capillary wicking until clogging, and reopening by polymer dissolution. Denoting the time scale of the former step as τ_w and the latter τ_d , their sum, $\tau = \tau_w + \tau_d$ corresponds to the period of the wicking process. If λ is the characteristic distance that a liquid travels before the conduit is clogged, the average wicking velocity is given by λ/τ . In the following, we show that the time for wicking and swelling

3.4 Completely soluble wicking

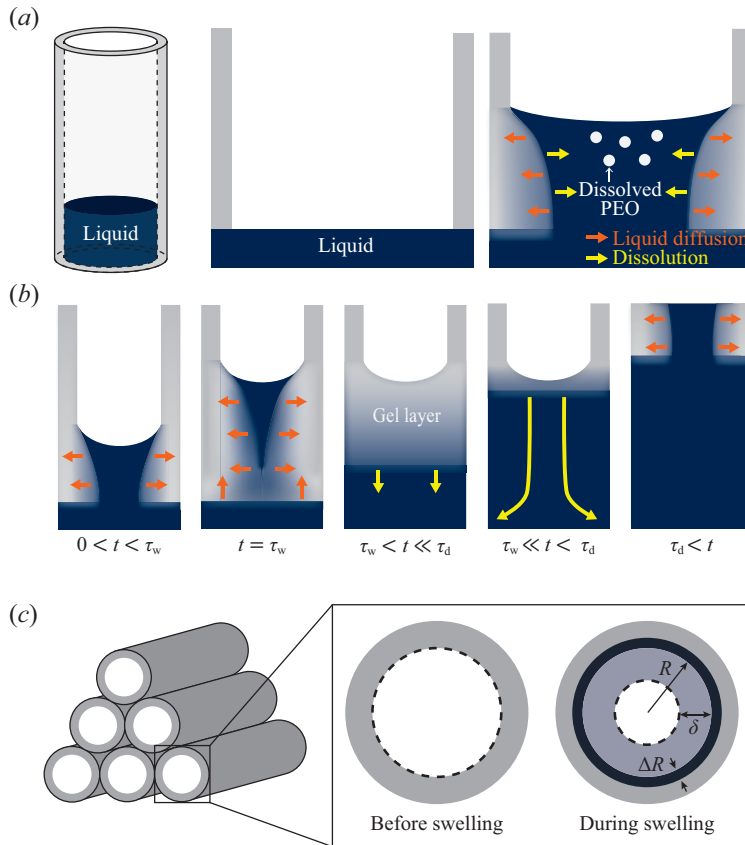


Figure 3.10: Schematic illustrations of solvent imbibition through a soluble capillary. (a) When the conduit is wide, the wicking velocity is an outcome of simultaneous interactions of capillary wicking, solvent diffusion into the wall, wall swelling, and dissolution. (b) When the conduit is narrow, the swelling polymer blocks the conduit rapidly. The wicking speed is determined by how fast the gel layer is dissolved into the liquid. (c) Schematics of pore clogging process in porous media, assumed as an assemblage of cylindrical conduits of equivalent radius R , due to solvent diffusion into polymeric wall. While the solvent diffuses into an inner wall of a single conduit by a distance ΔR , the conduit radius is reduced to $R - \delta$ due to the wall swelling as much as δ .

3.4 Completely soluble wicking

before clogging is much shorter than the dissolution time, i.e., $\tau_d \gg \tau_w$. Then we get $\tau \approx \tau_d$ because the dissolution is the rate-determining step, which allows us to find the wicking velocity to be λ/τ_d . Therefore, we only need to consider the rate of dissolution in order to find the wicking velocity rather than considering simultaneous wicking, swelling and dissolution.

Figure 3.9(c) schematically illustrates the processes during soluble wicking. While liquid infiltrates into the porous sheet, the fibers surrounding pores are swollen with diffusion of the solvent (liquid). Figure 3.9(d) shows the swelling of PEO fibers with absorption of water, leading to buckling and contacts of initially aligned fibers. In order for the wicking to resume after this pore clogging, a sufficient amount of polymer in the gel layer should be dissolved away into the fresh liquid following the wetting front. Therefore, the liquid transport in soluble porous media is an outcome of repeated processes of capillary wicking of a short distance accompanied by pore clogging and polymer dissolution.

The soluble wicking distance L_s for a time t significantly greater than τ is then written as $L_s = \lambda t/\tau$. To estimate λ and τ , we consider the two time scales relevant to the soluble wicking.

(1) Time for wicking and swelling until clogging, τ_w : The time, τ_w , for liquid to wick over a distance λ owing to capillarity with negligible inertia can be given by the Washburn rule (Washburn, 1921): $\lambda \sim (\sigma R \tau_w / \tilde{\mu})^{1/2}$, where $\tilde{\mu}$ is the average viscosity of liquid. As the liquid diffuses into PEO fibers, the polymer swells, so that the fluid conduit is clogged as schematically illustrated in figure 3.10(c). Assuming the porous media as assemblage of cylindrical conduits of equivalent radius R , we consider diffusion of solvent into the inner wall of a polymeric cylindrical tube by a distance ΔR . Then the polymer swells in a way that the conduit radius is reduced to $R - \delta$. It is known that PEO swells approximately 10 times by absorbing aqueous liquids (El-Hady *et al.*, 2004), so that $\Delta R/R \sim 0.1$ when the conduit is clogged ($\delta = R$). With the characteristic swelling time scale τ_w estimated as the diffusion time scale to a distance of $\Delta R = 0.1R$, we get $\tau_w \sim (0.1R)^2/D_s$.

3.4 Completely soluble wicking

Because the diffusion coefficients of liquids C to F into PEO fibers are of the order of $D_s \sim 10^{-9} \text{ m}^2 \text{ s}^{-1}$ (Barnes *et al.*, 1994; Vrentas & Duda, 1979), we find $\tau_w \sim 10^{-5} \text{ s}$ for $R \sim 10^{-6} \text{ m}$.

(2) Time for reopening by polymer dissolution, τ_d : The time for polymer dissolution in fresh liquid by disentanglement of loosened polymer chains is scaled as $\tau_d \sim \lambda/K_d$, where the unit wicking distance λ serves as a gel layer thickness, and K_d is the rate of polymer chain detachment and diffusion into liquid. If the diffusivity of a polymer in a liquid and the radius of gyration are respectively denoted as D_l and r_g , K_d is scaled as $K_d \sim D_l/r_g$ (Doi & Edwards, 1988; de Gennes, 1979). Using the Stokes-Einstein relation (Couper & Stepto, 1969), $D_l \approx k_B T / (6\pi\mu r_g)$ with k_B , T and μ respectively being the Boltzmann constant, the absolute temperature and the viscosity of fresh liquid, we estimate $\tau_d \sim 6\pi\lambda\mu r_g^2 / (k_B T)$.

As the capillary wicking stops due to pore clogging by swelling, the distance λ can be obtained by substituting $\tau_w \sim (0.1R)^2/D_s$ into the foregoing Washburn rule: $\lambda \sim 0.1R[\sigma R/(\tilde{\mu}D_s)]^{1/2}$. The viscosity of wicking liquid increases exponentially with the PEO concentration, and thus we take $\tilde{\mu} \sim 1 \text{ Pa}\cdot\text{s}$ based on the viscosity data of aqueous solution of PEO with molecular weight of $3 \times 10^5 \text{ g mol}^{-1}$ (Ebagninin *et al.*, 2009). Then, we find the gel layer thickness to scale as $\lambda_c \sim 10^{-6} \text{ m}$. This value is consistent with the thickness of a mushy layer formed at the wetting front radially emanating from a liquid source at the centre, as imaged by an inverted microscope (Nikon Eclipse TS100) in figure 3.9(e). We obtain the estimates of the time scales, $\tau_w \sim 10^{-5} \text{ s}$ and $\tau_d \sim 10^{-3} \text{ s}$ with a characteristic value of r_g taken to be 10^{-8} m (Werzer *et al.*, 2011). Therefore, the slowest polymer dissolution is a rate-limiting step that determines the rate of liquid invasion in soluble porous sheets of PEO fibers.

We write $L_s \sim \lambda t / \tau_d$, which gives

$$L_s \sim \frac{\beta}{\mu} t, \quad (3.8)$$

3.4 Completely soluble wicking

with $\beta = k_B T / r_g^2$. Figure 3.9(b) shows that the scattered data of liquid invasion distance L_s for various liquids are collapsed onto a single line when plotted according to scaling law (3.8). The slope of the line of best fit is $\alpha_s = 1.2$, leading us to write $L_s = \alpha_s \beta t / \mu$. The liquid invasion rate in soluble isotropic porous sheets is critically dependent on the viscosity but independent of surface tension of liquid, as the rate of disentanglement of polymer chains into fresh liquid determines the liquid propagation speed.

3.4.3 Control the soluble flow direction

As shown in figure 3.11(c-d), the completely soluble wicking tends to occur independent direction with spiky circular fronts. This uneven wet front is due to the varying thickness of the gel layer due to the irregular microstructure of the porous sheet composed of PEO nanofibers. Although the gel layer thickness is determined by liquid absorption including diffusion, we assume the formed gel layer thickness as the liquid's capillary wicking distance before clogging in our mathematical analysis of completely soluble wicking. This assumption is reasonable because soluble wicking rarely occurs in the direction where the liquid is highly diffusible within a fibrous PEO sheet. The absorbed liquids form a gel layer, and the polymer dissolution decreases its thickness. The liquid is absorbed into porous PEO sheets by capillary wicking before clogging, however, once the pore clogs, liquids cannot permeate through pores anymore but diffuses into PEO fiber itself. During the liquid absorption, liquids also keep dissolving the gel layer, so the total gel layer thickness λ_t at time t with $t = 0$ at pore clogging is $\lambda_c + \lambda_d - K_d t$, where the λ_c and λ_d are the gel layer thickness formed by liquid wicking and diffusion, respectively (see Figure 3.11(a)). The gel layer formed by wicking λ_c is the liquid invasion stopping distance that is the order of 10^{-6} m. Liquid diffusion flux follows the Fick's law written as $J = -D_s \nabla c$ with being ∇c the liquid concentration gradient corresponding to $-\Delta c / \lambda_t$. Right after pore-clogging, $\lambda_t = \lambda_c$, leading to $\lambda_d \sim D_s t / \lambda_c$. Thus, the rate of change in total gel layer thickness is given

3.4 Completely soluble wicking

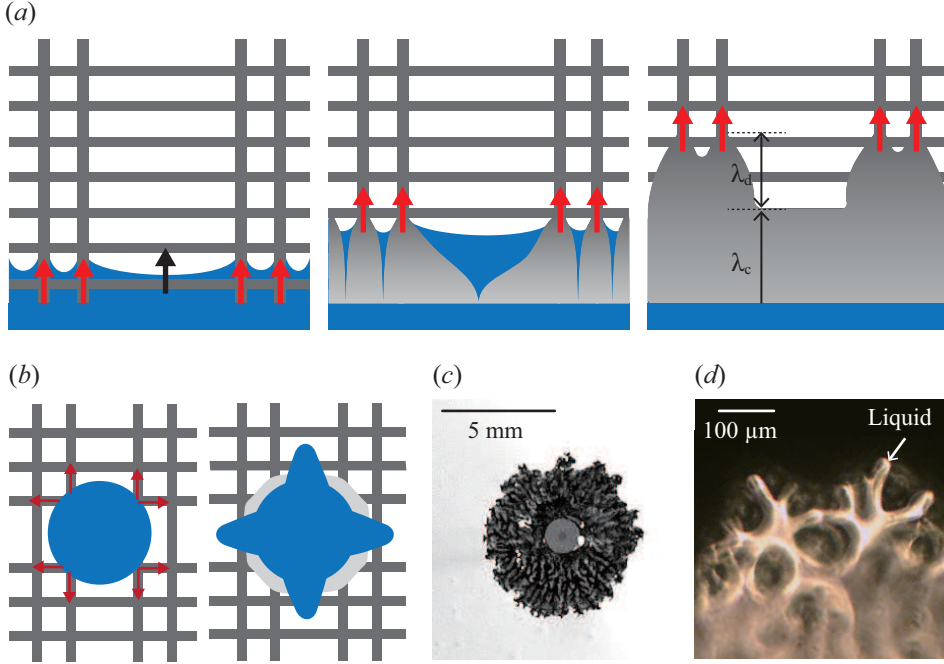


Figure 3.11: (a) Schematics of the gel layer formation in simply modelled porous sheet of randomly deposited soluble fibers. (b) Schematics of the location where the wicking resumes and stops. In the porous PEO sheets, the gel layer is retained in a direction having a microstructure of liquid diffusible so the wicking cannot resume, otherwise the wicking resumes. (c) Optical image of fully soluble wicking pattern and (d) Inverted microscopy image of it.

by $D_s/\lambda_c - K_d$. Because the diffusion coefficient of liquids D to G into PEO fibers is the order of $D_s \sim 10^{-9} \text{m}^2\text{s}^{-1}$ and the dissolution rate is the order of $K_d \sim 10^{-3} \text{ms}^{-1}$, the gel layer thickness is constant regardless of time. Thus, the gel layer will remain as long as the liquid can diffuse.

The porous PEO sheet composed of randomly deposited fibers can be simply modelled as woven structure having various gap distance between fibers as depicted in figure 3.11(b). When a liquid drop is deposited on the sheet, the liquid firstly invades into the gaps and forms a gel layer. This gel layer keeps its thickness in the direction where the liquid can diffuse so the resume of wicking process is terminally prohibited. The section in which

3.4 Completely soluble wicking

the wicking is suppressed is randomly deposited due to the randomness of the sheet's microstructure and it leads to the spiky soluble wicking pattern as shown in figure 3.11(c-d).

Completely soluble wicking in fibrous porous polymers dramatically inhibited in the directions with diffusible microstructure. Based on this finding, we devised a porous PEO sheet having a microstructure with extremely different diffusivity to control the direction of soluble wicking as depicted in figure 3.12(a). In the fibrous PEO sheets composed of aligned fibers, liquids easily diffuse into fiber lengthwise direction along the fiber itself, whereas it hardly diffuses into fiber crosswise direction due to the media's discreteness. The fibrous PEO sheets composed of aligned fibers are fabricated by electrospinning with same condition as the randomly deposited fibrous PEO sheets except for the collector that is the drum collector rotating at the same linear speed as the jet (4.7 ms^{-1}) (Shin *et al.*, 2018), as shown in figure 3.12(a). The average thickness of the sheets obtained by the directional electrospinning process was $33 \text{ }\mu\text{m}$. The average radius of fibers was measured using SEM (scanning electron microscopy) images, and the porosity was obtained by comparing the densities of PEO and the fibrous sheets. The characteristics of the fibrous sheets are listed in table 3.2. The average distance between aligned fibers in the directionally electrospun substrates was measured via SEM images to be $7 \text{ }\mu\text{m}$ with the standard deviation of $3 \text{ }\mu\text{m}$. In appendix A, we observe the insoluble flow in the fibrous PEO sheets composed of directionally aligned fibers and compare it to that in the fibrous PEO sheets composed of randomly aligned fibers in order to analyze the wicking characteristics of the directional sheets.

To check the soluble wicking pattern on the porous sheets of directionally deposited PEO fibers, we observed the wicking of a liquid emanated from a capillary tube likewise the observation at the porous sheets of randomly deposited PEO fibers in chapter 3.5.1. As we intended, the liquid wicks much faster in the crosswise direction than the lengthwise direction,

3.4 Completely soluble wicking

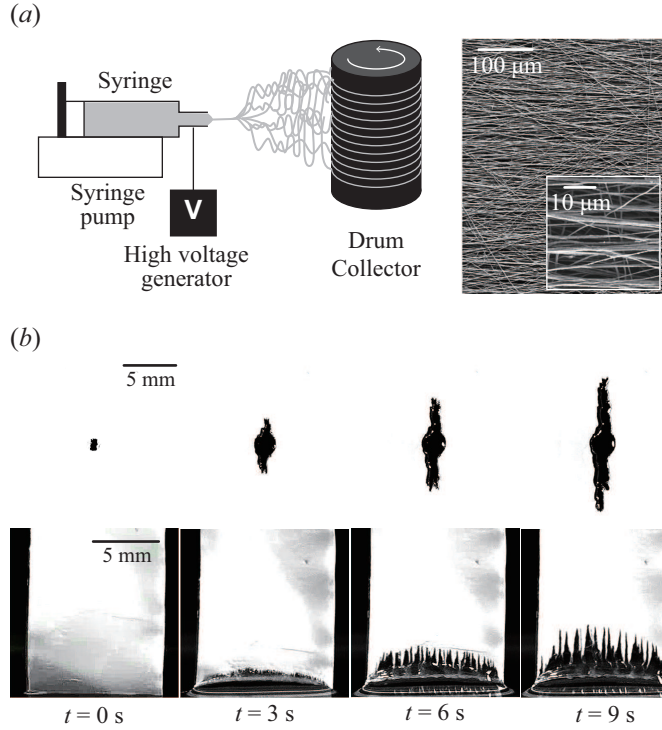


Figure 3.12: (a) Schematic illustration of the fabrication of the porous sheets composed of directionally aligned PEO nanofibers using electrospinning, and the corresponding SEM image. (b) Wicking of water in a soluble sheet composed of directionally deposited nanofibers. In (b), the up and down rows correspond to the flows from a point sourced (capillary) and a liquid pool, respectively.

Fiber radius, R_f , \pm std (nm)	234 ± 50
Porosity, ϕ	0.65
Equivalent pore radius, R (μm)	0.86
Permeability, k , measured (m^2)	4.1×10^{-15}
Permeability, k , modeled (m^2)	4.4×10^{-15}

Table 3.2: Characteristics of the porous fibrous sheets. In fiber radius, std stands for standard deviation.

3.4 Completely soluble wicking

thus the wet area growing from a point source elongates in a direction perpendicular to aligned fibers while the wicking along the fibers is severely suppressed as shown in the up row of figure 3.12(b). The wetting front advancing from a liquid pool's free surface is fairly spiky when the free surface and the fiber directions are parallel, as shown in the down row of figure 3.12(b). Wicking was hardly observed when the strip touched the free surface with the fiber direction perpendicular to the free surface. Then, we measure the rate of one-dimensional wicking to compare the liquid invasion mechanism in the directionally deposited sheets to that in the randomly deposited sheets. We only plot the wicking distance in crosswise direction, L_d , versus time in figure 3.13(a) since the lengthwise wicking in directionally deposited fibrous soluble sheets is insignificant. The distance corresponds to the average height of spiky fronts shown in the up row of figure 3.12(b). We see that the distance grows linearly with time just as for the randomly deposited sheets but at a higher rate. Since the coupled process of pore invasion–pore clogging–polymer dissolution should still arise for liquid propagation, we plot L_d versus $\beta t/\mu$ according to scaling law (3.8) in figure 3.13(b). We find the experimental data to be collapsed onto a single line with a slope, $\alpha_d = 1.6$ which is 1.3 times higher than the value for the randomly deposited sheets, α_s .

To understand why the wicking of reactive liquids is fast in the crosswise direction but severely suppressed in the lengthwise direction, we schematically illustrate physical processes during crosswise and lengthwise wicking in figure 3.13(c) and (d), respectively. When the liquid front and fiber alignment are parallel, figure 3.13(c), the dissolved polymer chains can be easily carried away by fresh liquid that follows the wicking front. The aligned but buckled fibers having a number of contacts with neighbours guide the flow to occur perpendicular to the fiber alignment direction without detouring, in contrast with randomly deposited, insoluble unswollen fibers that force the flow to detour in seeking easy supply path of fresh liquid. The unevenness of wet front shown in figure 3.11(c–d) reflects such detouring in

3.4 Completely soluble wicking

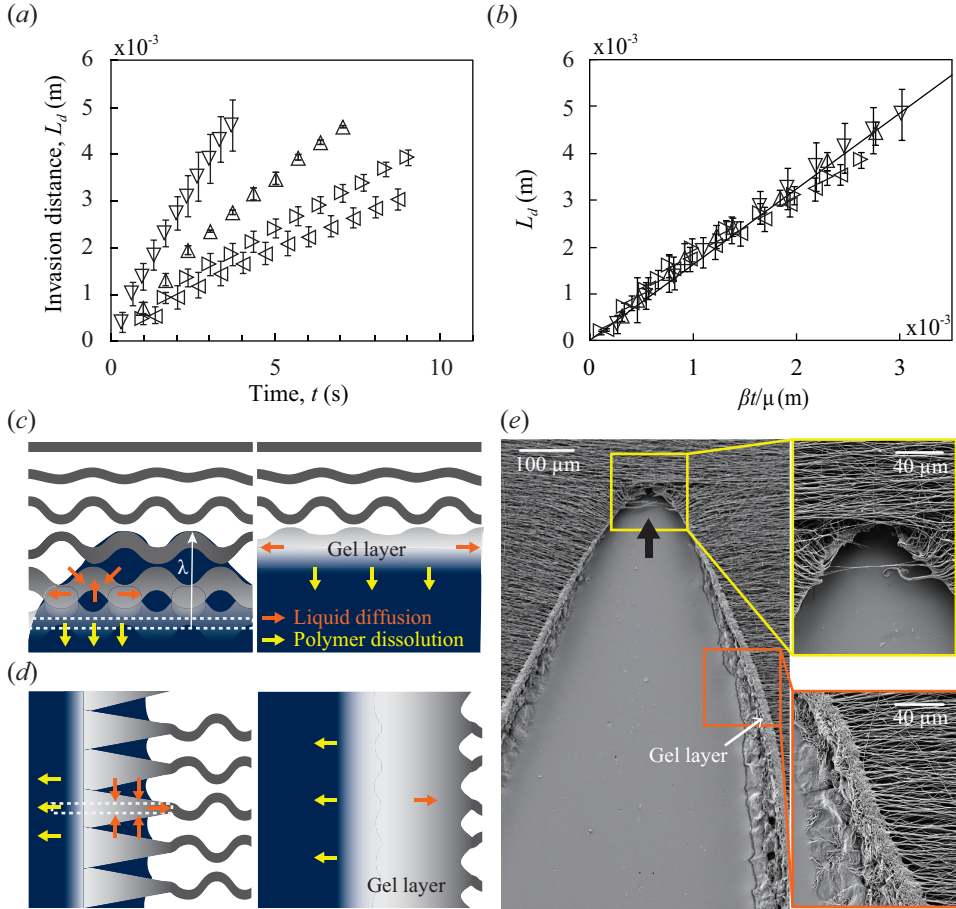


Figure 3.13: (a) The liquid invasion distance, L_d , of various liquids versus time in soluble porous sheets of directionally deposited PEO fibers. (b) L_d versus $\beta t/\mu$, plotted according to scaling law (3.8). Schematics of physical processes during wicking in (c) the crosswise and (d) the lengthwise direction. (e) SEM images of a sheet of directionally deposited fibers after wicking of water emanated from a capillary.

randomly deposited substrates. The polymer dissociation is still the limiting step in liquid wicking, allowing us to write $L_d = \alpha_d \beta t / \mu$. We consider the ratio α_d / α_s a measure of randomness of fiber directionality affecting the invasion rate of liquid in soluble fibrous sheets.

When liquid attempts to flow in the lengthwise direction, figure 3.13(*d*), the aligned fibers are continually dissolved into the diffusing solvent forming an excessively thick gel layer, which cannot meet fresh liquid to remove disentangled polymer chains. The thick gel layer blocking the lengthwise invasion is clearly observed in an SEM image taken after a wicking test, figure 3.13(*e*). The tip of the opening area shows a thin gel layer of the order of 10^{-6} m, facilitating the crosswise wicking to elongate the opening in the direction designated by the black arrow. Such pointed propagation of liquid while shielded by thick gel layer in the sides appears to result in the highly spiky wet front in the down row of figure 3.12(*b*).

3.5 Conclusion

We have shown both experimentally and theoretically that the wicking dynamics of liquids in fibrous sheets are qualitatively different depending on whether the fibres' solubility. In partially soluble wicking regime, we found that the imbibition with dissolution is distinctively slower than without dissolution. We have rationalized the observations by developing a mathematical model that explains how dissolution affects the liquid viscosity and thus the imbibition velocity. The model can be directly used for liquid absorption through porous media made of a wide range of polymers. Our study not only provides a theoretical framework to analyze the dynamics of liquid infiltration through partially soluble polymeric porous media, but also can potentially help us to control the long-term drug delivery system and the decontamination process of polymeric contaminants in soil.

In a completely soluble wicking regime, the wicking dynamics are limited by the dissolution rate of polymer chains into liquid, so the wicking

3.5 Conclusion

distance grows linearly with time in randomly deposited fibrous sheets. Although capillarity-driven imbibition in insoluble fibrous media is governed by such physical properties as surface tension and viscosity of liquid and porosity and permeability of porous network, our study of soluble porous media reveals that their wicking dynamics are mainly determined by viscosity. However, the possibility of completely soluble wicking is related to the gel layer thickness over time, governed by the microstructure of fibrous PEO sheets. In the direction having high diffusivity within fibrous PEO sheets, the gel layer retains for a long time, thus the wicking rarely resumes. Based on this, we devised a strategy to control the soluble wicking pattern by controlling the microstructure of fibrous sheets and verified this strategy with the directionally deposited fibrous sheets. We found that the constant wicking rate also holds for the crosswise wicking in directionally deposited soluble fibrous sheets. But the lengthwise propagation is inhibited by excessively thick gel layers formed by continual diffusion of solvent along the aligned fibers. In particular, the high sensitivity of soluble wicking rates to the orientation of fiber alignment opens a new pathway to accurately control the dissolution behavior of porous sheets. One can expedite the dissolution of porous shells by arranging fibers perpendicular to the desired wicking direction (to induce crosswise wicking) while arranging fibers parallel to the undesired direction. It is also possible to spatially pattern the orientation of fibers so that the wicking can occur along a designated path. In practice, such a delicate scheme of guided dissolution will help one to design air-trapping porous drug delivery systems (Singh & Kim, 2000; Yuasa *et al.*, 1996) capable of releasing drugs at a precisely controlled rate and direction, to encrypt messages on a soluble piece of paper (Burgess *et al.*, 2011; Thomas *et al.*, 2009), or to devise soft robots capable of actuation or morphing in response to surrounding chemical environments (Yang *et al.*, 2018).

Chapter 4

Concluding remarks

In this chapter, we first summarize the main findings of our research in §4.1. Then, we suggest possible directions for future research that are motivated by experimental and theoretical results of this thesis in §4.2.

4.1 Summary of findings

We have theoretically and experimentally investigated the deformation dynamics of porous polymers induced by liquids. The deformation of porous polymers can be classified into swelling and dissolution. Firstly, as the swelling dynamics problem of porous polymer, we investigated the hydrogel system whose actuation is driven by the swelling of porous polymers. Next, we studied the wetting and dissolution in the polymer sheets composed of nanofibers with various solubilities as the dissolution dynamics problem of porous polymers.

In chapter 1, we first divide the liquid transport into two manners according to its thermodynamical compatibility with porous polymers: wicking and diffusion, and briefly reviewed the fundamental theories of wicking in porous media, on which our theoretical development will be based. We also reviewed the recent studies about the wicking with deformation occurring by diffusion of liquids into the media itself.

4.1 Summary of findings

In chapter 2, we investigated the fast and strong electro-active hydrogel system actuating by swelling. We first introduced the weaknesses of hydrogels limiting their application scopes which are fragility to compression and slow response. We developed a fast and powerful force generation system driven by porous polymer swelling. We manufactured this system by encasing a hydrogel with a stiff membrane having a limited volume to expand and significantly accelerated the operating speed of strong hydrogel systems by applying the electric field. By measuring the force generation of this hydrogel system, referred to as a strong hydrogel system, and the water mass uptaken of a bare electro-active hydrogel over time, we showed the strength and fast reaction of this system. Here, we conjectured the operation principle of the strong hydrogel system as the net volume change of a confined hydrogel, and then we experimentally and theoretically studied the swelling and deswelling dynamics of electro-active nanoporous hydrogel in electric fields. We revealed that the swelling of electro-active hydrogel is quickened and enlarged within electric fields due to electroosmosis and also discovered the deswelling rate given by Darcy's law based on the theory of effective stress in saturated porous media. Finally, we estimated the force generation in strong hydrogel systems within different electric fields by combining the swelling and deswelling rate of an electro-active hydrogel. The estimated force is well matched with the experimental results, and this resulted in the conclusion that the force generation rate is determined by the strength of the applied electric field, and the maximum force generated by the hydrogel system is limited by the hydrogel swelling rate and membrane stiffness.

In chapter 3, we studied the dissolution dynamics in porous polymers, a representative problem involving wetting and dissolution of polymeric porous media. To be specific, we experimentally and theoretically studied the wicking dynamics of liquids in fibrous polymer sheets depending on the fiber's solubility. As a model system to study the dynamics of soluble wicking depending on the fiber's solubility, we use porous sheets composed of electrospun polyethylene oxide fibers contacting with various liquids like

4.1 Summary of findings

this. First of all, we classified the soluble wicking regime into partially soluble wicking and completely soluble wicking. In the study of the partially soluble wicking regime, we observed the wicking distance in fibrous PEO sheets that absorb an aqueous EG mixture from the bottom. Although the partially soluble wicking is slower than expected by Darcy's law, it shows diffusive behavior, likewise the insoluble wicking ($L \sim t^{1/2}$). We estimated the effect of polymer dissolution in partially soluble wicking into three manners: the change of pore size, surface tension, and viscosity. With various experiments and theoretical analysis, we concluded that the low speed of partially soluble wicking stems from the viscosity increase due to the dissolution of the polymer. In the study of a completely soluble wicking regime, we observed the wicking distance in fibrous PEO sheets that absorb an aqueous EG mixture and chloroform from the bottom and the wicking pattern generated by a liquid from a point source emanating from a capillary tube touching a PEO fibrous sheet. Unlike the insoluble and partially soluble wicking, the rate of complete soluble wicking is determined by a completely different process. With an observation of the completely soluble wicking process with microscope and SEM, we discovered the formation of the gel layer, which strongly prevents the liquid transport through the pores during the completely soluble wicking, and the completely soluble wicking is an outcome of repeated processes of capillary wicking of a short distance accompanied by pore clogging and polymer dissolution. Thus, the wicking dynamics are limited by the dissolution rate of polymer chains into liquid, so the wicking distance grows linearly with time in randomly deposited fibrous sheets. Although capillarity-driven imbibition in insoluble fibrous media is governed by such physical properties as surface tension and viscosity of liquid and porosity and permeability of porous network, our study of soluble porous media reveals that their wicking dynamics are mainly determined by viscosity. However, the possibility of completely soluble wicking that determines the wicking pattern is related to the gel layer thickness over time, governed by the microstructure of fibrous PEO sheets.

In the direction having high diffusivity within fibrous PEO sheets, the gel layer retains for a long time, thus the wicking rarely resumes. Based on these findings, we devised a strategy to control the soluble wicking pattern by controlling the microstructure of fibrous sheets and verified this strategy with the directionally deposited fibrous sheets. We found that the constant wicking rate also holds for the crosswise wicking in directionally deposited soluble fibrous sheets.

4.2 Future works

As we summarized in §4.1, we experimentally and theoretically explored the mechanics of *fluid* flow and *polymer* deformation in the porous polymer. Although we captured the fundamental physics related to polymer deformations in liquids, one might need to be equipped with further research to apply it in practice. In the following, we suggest several possible future works related to this study.

Hydrogel system with reversibly changeable mechanical properties

The strong hydrogel systems, we suggested in chapter 2, actuates with the hydrogel swelling, and this system's mechanical properties are determined by the filling ratio of hydrogel inside the membrane. Here, the swelling and deswelling process of hydrogels are reversible. To apply the strong hydrogel system as a system with reversibly changeable mechanical properties, the analysis of mechanical properties according to the filling ratio of hydrogel inside the membrane needs to be performed. Further experimental exploration is also necessary to control the swelling and deswelling of a hydrogel. We anticipate that the system with reversibly changeable mechanical properties has the potential to surgical robots or marine rescue robots, which require stiffness at a certain limited moment.

Origami hydrogel system

Origami, a form of art that traces its roots in ancient Japan, has its presence been spotted in the industrial context as it has been discovered to have amazing new capabilities in adding indispensable mechanical attributes to deployable and foldable structures. We expect that the origami structure facilitates large deformation of a strong hydrogel system, so opens new possibilities in harsh conditions like the space environment where a combination of maneuverability and durability is a necessary feature.

Smart drug

Although we have successfully enhanced the understanding of the soluble wicking in porous polymers and devised the microstructure of a membrane to control the soluble wicking rate, one limitation of our research in the polymer dissolution dynamics is that the investigations were limited in the two-dimensional structure. To apply our findings to practice in areas such as drug delivery, further efforts are required to design and fabricate a three-dimensional diffusivity controllable structure. As we reported in chapter 3, the penetration speed of liquids is determined by the diffusivity of the porous polymer, thus we anticipate that the drug's time-controlled release is possible with the porous polymer having three-dimensional diffusivity controllable structure. Furthermore, the drug having more than two different time scales of dosage might be producible by controlling the local microstructure of drugs.

Appendix A

Non-soluble wicking in directional porous sheets

The wicking whose dynamics change sensitively to directionality of porous network as well as the solid's solubility. As a model system to study the dynamics of wicking in different porous networks, we used sheets of fibers of PEO which were produced by electrospinning. By controlling the orderliness of fibres in the fibre deposition process, we can investigate the effects of fibre directionality (random or directional) on the preferred orientation and rates of wicking dynamics. A jet of aqueous PEO solution was ejected from a metal capillary under the strong electric field and partially solidified during flight and deposited on a collector as fibers. On a flat plate ground, the fibers were chaotically deposited, whereas the fibers were aligned in one direction on a surface of a drum collector rotating as shown in figure A.1(*a-b*). In figure A.1(*b*), we find some fibres crossing the uniformly aligned fibres, which play an important role to guide wicking in some cases as discussed below.

We observed wicking of non-dissolving liquids (Liquids A and B) emanated from a capillary tube on a porous substrate due to capillary action

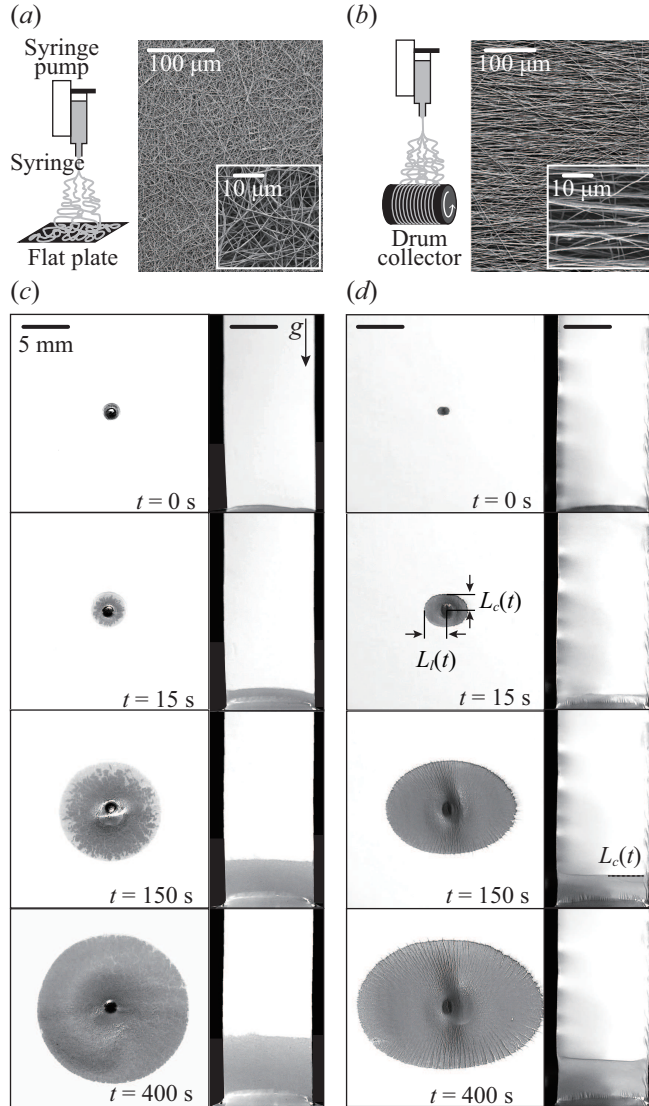


Figure A.1: (a) Random deposition of electrospun fibres of PEO, and the corresponding SEM image. (b) Directional deposition of electrospun fibres of PEO, and the corresponding SEM image. (c) Wicking of a liquid from a point source emanating from a capillary tube touching a PEO fibrous sheet. (d) Propagation of liquid front against gravity into a strip of fibrous PEO sheet.

to check the directionality of the spreading dynamics and separately measured the rate of one-dimensional wicking by observing the propagation of wetting front, $L(t)$, in a 1 cm wide strip from the free surface of a liquid pool. When the fibers are randomly deposited and insoluble in the liquid, the wicking occurs independent of direction exhibiting a circular wet area growing from a point source as shown in the left column of figure A.1(c). For the insoluble strip contacting a free surface of the liquid, a horizontal wetting front advances against the direction of gravity as shown in the right column of figure A.1(c). However, when the fibers are aligned and insoluble, the liquid wicks faster along the fiber direction than across the direction. Thus, the wet area growing from a point source is elliptical with the major axis coinciding with the fiber alignment direction, as shown in the left column of figure A.1(d). Relatively smooth horizontal wetting front propagates from a free surface as shown in the right column of figure A.1(c) with the speeds different depending on the orientation of fibers relative to a free surface of liquid.

We plot the wicking distance of liquids A and B in the sheets of randomly deposited fibers in figure A.2(a). Although the wicking occurs at different rates for the differing properties of the liquids (inset in the figure), the measurement data of wicking distance are collapsed onto a single line when plotted according to (3.1). The diffusive behavior of the wetting distance on two-dimensionally isotropic insoluble porous sheets is consistent with prior studies using fibrous sheets of nonwoven fabrics (Kim *et al.*, 2015) and paper (Kim *et al.*, 2011). The slope of the best-fitting dotted line in figure A.2(c) corresponds to $4k_r/\phi$, and we find the permeability of the insoluble porous sheet of randomly deposited fibers to be $k_r = 4.8 \times 10^{-14}$ m².

We now consider the wicking rates in the sheets of directionally deposited fibres as shown in figure A.1(d). As the wicking rate depends on the direction of flow relative to fibre alignment, we plot the temporal evolutions of the lengthwise imbibition L_l and the crosswise imbibition

tion L_c in figure A.2(b). We see different power laws observed depending on the wicking direction, so that $L_l \sim t^{1/2}$ and $L_c \sim t^{1/3}$. The diffusive behaviour of L_l indicates that the lengthwise flow follows Darcy's law as driven by capillarity. Thus, we express L_l in the same form as (3.1), $L_l = 2[(1 - \phi)k_l\sigma/(\phi^2 R_f \mu)]^{1/2} t^{1/2}$ with k_l being the permeability of the directionally deposited sheet, which collapses the raw data of L_l of liquids A and B onto a single line, as shown in figure A.2(c). The slope of the line of best fit empirically gives the permeability, $k_l = 4.1 \times 10^{-15} \text{ m}^2$.

Given the measured values of permeability in random and directional fibrous sheets, we check whether they can be predicted by a previous model (Rodriguez *et al.*, 2004) which proposes the following form of k as a function of porosity: $k = \phi^{n+1}(1 - \phi)^{-n}/C$, where n and C are empirical parameters. Taking $n = 0.97$, a value corresponding to fibre glass in Rodriguez *et al.* (2004), we find $C = 2.6 \times 10^{14} \text{ m}^{-2}$ to match the measured and predicted permeabilities of a random deposited sheet, $k_r = 4.8 \times 10^{-14} \text{ m}^2$. The chosen values of n and C lead to the following value of the permeability in the directionally deposited sheet predicted: $k_l = 4.4 \times 10^{-15} \text{ m}^2$, which matches closely the measured value of $k_l = 4.1 \times 10^{-15} \text{ m}^2$. This is consistent with the previous finding (Rodriguez *et al.*, 2004) that the permeability of porous media made of the same fibre materials exhibits the same functional dependency on porosity whether fibres are aligned or not.

For imbibition to arise in the crosswise direction, the liquid following the aligned fibres should either touch adjacent fibres upon bulging through the inter-fibre gaps (Bayramli & Powell, 1990) or wick along misaligned fibres crossing the fibre alignments. Because the average inter-fibre distance (7 μm) is greater than fibre radius (235 nm), the bulging is unlikely to convey liquid to adjacent fibres. Thus, the flow path for the crosswise impregnation is provided by occasionally encountered misaligned fibres, as schematically shown in the inset of figure A.2(d). Since the pathway of crosswise wicking involves complex detours, the wicking dynamics no longer follows the classical diffusive rule.

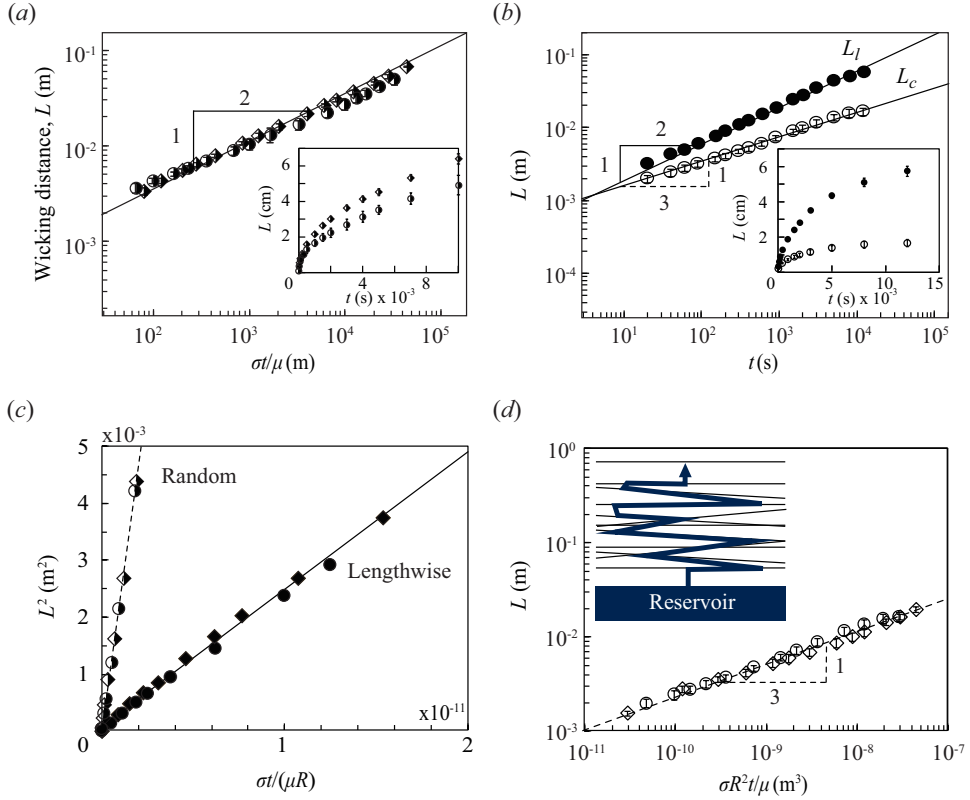


Figure A.2: (a) The wicking distance of liquids A and B in insoluble porous sheets of randomly deposited fibres plotted according to (3.1). Inset: Raw data of L versus t . (b) The wicking distance of liquid A in insoluble sheets of directionally deposited fibres. Different power laws are observed depending on the flow direction. Inset: Linear plots of L_l and L_c versus t . (c) The wicking distances in insoluble sheets of randomly deposited fibres, and the lengthwise wicking distances in insoluble sheets of directionally deposited fibres, plotted according to scaling law (3.1). The slopes of the best fitting lines corresponding to $4k_r/\phi$ are 2.3×10^{-13} and 2.5×10^{-14} m² for random and directional substrates, respectively. (d) The crosswise wicking distance of liquids A and B plotted versus $\sigma R t / \mu$.

With no theoretical models for the crosswise wicking available, we figure out the functional dependence of wicking distance on such independent parameters as t , R , σ and μ based on dimensional analysis (Buckingham, 1914). The dimensionless crosswise wicking distance L_c/R is a function of a dimensionless time, $\sigma t/(\mu R)$. Assuming that a power law is observed, we write $L_c \sim (\sigma t/\mu)^\alpha R^{1-\alpha}$. We have seen that $\alpha = 1/2$ for insoluble wicking in randomly deposited sheets and lengthwise imbibition in directional fibrous sheets above. However, for crosswise wicking that suffers from infrequent but tortuous flow paths, α tends to decrease with the increase of the tortuosity, defined as the length ratio of the actual flow path to the straight path (Cai & Yu, 2011). The tortuosity will increase as the number of misaligned fibres decreases. Upon finding that $L_c \sim t^{1/3}$ from our raw data, we have plotted L_c versus $\sigma R^2 t/\mu$ in figure A.2(d), which validates that the power law is indeed observed with a power $\alpha = 1/3$ for the particular fibrous sheets used in this work.

References

- BARNES, A. C., BIEZE, T. W. N., ENDERBY, J. E. & LEYTE, J. C. 1994 Dynamics of water in the poly (ethylene oxide) hydration shell: a quasi elastic neutron-scattering study. *J. Phys. Chem.* **98** (44), 11527–11532.
- BAVER, L. D. 1949 *Retension and movement of soil moisture*. Hydrology. Dover Pubs.
- BAYRAMLI, E. & POWELL, R. L. 1990 The normal (transverse) impregnation of liquids into axially oriented fiber bundles. *J. Colloid Interface Sci.* **138** (2), 346–353.
- BEAR, J. 1972 *Dynamics of Fluid in Porous Media*. Elsevier.
- BIRD, R. B., STEWART, W. E. & LIGHTFOOT, E. N. 2006 *Transport Phenomena, revised 2 nd edition*. John Wiley & Sons, Inc New York.
- BRAZEL, C. S. & ROSEN, S. L. 2012 *Fundamental Principles of Polymeric Materials*. Hoboken: Wiley.
- BRIELLES, N., CHANTRAINE, F., VIANA, M., CHULIA, D., BRANLARD, P., RUBINSTENN, G., LEQUEUX, F., LASSEUX, D., BIROT, M., ROUX, D. & MONDAIN-MONVAL, O. 2007 Imbibition and dissolution of a porous medium. *Ind. Eng. Chem. Res.* **46** (17), 5785–5793.
- BUCKINGHAM, E. 1914 On physically similar systems; illustrations of the use of dimensional equations. *Phys. rev.* **4** (4), 345.

REFERENCES

- BURGESS, I. B., MISHCHENKO, L., HATTON, B. D., KOLLE, M., LONCAR, M. & AIZENBERG, J. 2011 Encoding complex wettability patterns in chemically functionalized 3d photonic crystals. *J. Am. Chem. Soc.* **133** (32), 12430–12432.
- CAI, J. & YU, B. 2011 A discussion of the effect of tortuosity on the capillary imbibition in porous media. *Transp. Porous Media* **89** (2), 251–263.
- CALÓ, E. & KHUTORYANSKIY, V. V. 2015 Biomedical applications of hydrogels: A review of patents and commercial products. *Eur. Polym. J.* **65**, 252–267.
- CARMAN, P. C 1941 Capillary rise and capillary movement of moisture in fine sands. *Soil Sci.* **52** (1), 1–14.
- CARTA, M., MALPASS-EVANS, R., CROAD, M., ROGAN, Y., JANSEN, J. C., BERNARDO, P., BAZZARELLI, F. & MCKEOWN, N. B. 2013 An efficient polymer molecular sieve for membrane gas separations. *Science* **339** (6117), 303–307.
- CHAN, A. W. & NEUFELD, R. J. 2009 Modeling the controllable pH-responsive swelling and pore size of networked alginate based biomaterials. *Biomaterials* **30** (30), 6119–6129.
- CHAO, T. T. 1984 Use of partial dissolution techniques in geochemical exploration. *J. Geochem. Explor.* **20** (2), 101–135.
- CHEN, J. U. N. & PARK, K. 1999 Superporous hydrogels: Fast responsive hydrogel systems. *J. Macromol. Sci. A.* **36** (7-8), 917–930.
- CHIPPADA, U., YURKE, B. & LANGRANA, N. A. 2010 Simultaneous determination of young's modulus, shear modulus, and poisson's ratio of soft hydrogels. *J. Mater. Res.* **25** (3), 545–555.

REFERENCES

- COLOMBO, P., BETTINI, R., SANTI, P., DE ASCENTIIS, A. & PEPPAS, N. A. 1996 Analysis of the swelling and release mechanisms from drug delivery systems with emphasis on drug solubility and water transport. *J. Control. Release* **39** (2), 231–237.
- CORNELL, D. & KATZ, D. L. 1953 Flow of gases through consolidated porous media. *Ind. Eng. Chem. Res.* **45** (10), 2145–2152.
- COUPER, A. & STEPTO, R. F. T. 1969 Diffusion of low-molecular weight poly (ethylene oxide) in water. *T. Faraday Soc.* **65** (2486-2496).
- CUCCIA, N. L., POTHINENI, S., WU, B., MÉNDEZ HARPER, J. & BURTON, J. C. 2020 Pore-size dependence and slow relaxation of hydrogel friction on smooth surfaces. *PNAS* **117** (21), 11247–11256.
- DACCORD, G. 1987 Chemical dissolution of a porous medium by a reactive fluid. *Phys. Rev. Lett.* **58** (5), 479–482.
- DANIEL, D., GOH, S. S., TRUONG, T. N. B., KOH, X. Q. & TOMCZAK, N. 2021 Origin of underwater oil-repellence in polyelectrolyte brush surfaces. *Adv. Mater. Interfaces* **8** (2), 2001203.
- DARCY, H. 1856 *Les Fontaines publiques de la ville de Dijon*. Dalton.
- DOI, M. & EDWARDS, S. F. 1988 *The theory of polymer dynamics*, , vol. 73. oxford university press.
- DONG, J., ZHANG, K., LI, X., QIAN, Y., ZHU, H., YUAN, D., XU, Q.-H., JIANG, J. & ZHAO, D. 2017 Ultrathin two-dimensional porous organic nanosheets with molecular rotors for chemical sensing. *Nat. Commun.* **8** (1), 1–14.
- DUPOIT, J. 1863 *Études théoriques et pratiques sur le mouvement des eaux dans les canaux découverts et à travers les terrains perméables*. Dunod (Paris).

REFERENCES

- EBAGNININ, K. W., BENCHABANE, A. & BEKKOUR, K. 2009 Rheological characterization of poly (ethylene oxide) solutions of different molecular weights. *J. Colloid Interface Sci.* **336** (1), 360–367.
- EL-HADY, A., EL-REHIM, A., HASSAN, A. & ... 2004 Production of prednisolone by pseudomonas oleovorans cells incorporated into pvp/peo radiation crosslinked hydrogels. *J. Biomed. Biotechnol.* **2004** (4), 219–226.
- FANG, Q., WANG, J., GU, S., KASPAR, R. B., ZHUANG, Z., ZHENG, J., GUO, H., QIU, S. & YAN, Y. 2015 3d porous crystalline polyimide covalent organic frameworks for drug delivery. *J. Am. Chem. Soc.* **137** (26), 8352–8355.
- FORCHHEIMER, P. 1986 Über die ergiebigkeit von brummen, anlagen und sickerschlitzen. *Zeitsch Archit. Ing. Ver., Hannover* **32**, 539–563.
- GELLER, J. T. & HUNT, J. R. 1993 Mass transfer from nonaqueous phase organic liquids in water-saturated porous media. *Water Resour. Res.* **29** (4), 833–845.
- DE GENNES, P. G. 1979 *Scaling concepts in Polymer Physics*. Cornell University Press.
- DE GENNES, P.-G., BROCHARD-WYART, F. & QUÉRÉ, D. 2004 Capillarity and gravity. In *Capillarity and wetting phenomena*, pp. 33–67. Springer.
- GRIFFITHS, J. C. 1952 Grain-size distribution and reservoir-rock characteristics1. *AAPG Bull.* **36** (2), 205–229.
- GU, C., HUANG, N., CHEN, Y., QIN, L., XU, H., ZHANG, S., LI, F., MA, Y. & JIANG, D. 2015 π -conjugated microporous polymer films: designed synthesis, conducting properties, and photoenergy conversions. *Angew. Chem.* **127** (46), 13798–13802.

REFERENCES

- GU, C., HUANG, N., CHEN, Y., ZHANG, H., ZHANG, S., LI, F., MA, Y. & JIANG, D. 2016 Porous organic polymer films with tunable work functions and selective hole and electron flows for energy conversions. *Angew. Chem. Int. Ed.* **55** (9), 3049–3053.
- GU, C., HUANG, N., GAO, J., XU, F., XU, Y. & JIANG, D. 2014 Controlled synthesis of conjugated microporous polymer films: versatile platforms for highly sensitive and label-free chemo-and biosensing. *Angew. Chem. Int. Ed.* **53** (19), 4850–4855.
- HA, J., KIM, J., JUNG, Y., YUN, G., KIM, D.-N. & KIM, H.-Y. 2018 Poro-elasto-capillary wicking of cellulose sponges. *Sci. Adv.* **4** (3), eaao7051.
- HILDEBRAND, J. H. & SCOTT, R. S. 1950 *The solubility of nonelectrolytes*. New York: Rheinhold Publishing.
- HU, R. Y. Z., WANG, A. T. A. & HARTNETT, J. P. 1991 Surface tension measurement of aqueous polymer solutions. *Exp. Therm. Fluid Sci.* **4** (6), 723–729.
- HU, Y., ZHAO, X., VLASSAK, J. J. & SUO, Z. 2010 Using indentation to characterize the poroelasticity of gels. *Appl. Phys. Lett.* **96** (12), 121904.
- ISHIGURO, S. & HARTNETT, J. P. 1992 Surface tension of aqueous polymer solutions. *Int. Commun. Heat Mass* **19** (2), 285–295.
- JACOB, C. E. 1946 Radial flow in a leaky artesian aquifer. *EOS* **27** (2), 198–208.
- JAHANSHAHI-ANBUHI, S., HENRY, A., LEUNG, V., SICARD, C., PENNINGS, K., PELTON, R., BRENNAN, J. & FILIPE, C. 2013 Paper-based microfluidics with an erodible polymeric bridge giving controlled release and timed flow shutoff. *Lab chip* **14**.

REFERENCES

- JUNG, S., KIM, W. & KIM, H.-Y. 2020 Dynamics of liquid imbibition through partially soluble porous sheets. *JMST Advances* **2** (3), 53–59.
- JUNG, S., KIM, W. & KIM, H.-Y. 2021 Dynamics of directional soluble wicking. *J. Fluid Mech.* **915**.
- KIM, J., HA, J. & KIM, H.-Y. 2017 Capillary rise of non-aqueous liquids in cellulose sponges. *J. Fluid Mech.* **818**, R2.
- KIM, J., MOON, M.-W., LEE, K.-R., MAHADEVAN, L. & KIM, H.-Y. 2011 Hydrodynamics of writing with ink. *Phys. Rev. Lett.* **107** (26), 264501.
- KIM, S. & LEE, Y. M. 2015 Rigid and microporous polymers for gas separation membranes. *Prog. Polym. Sci.* **43**, 1–32.
- KIM, S. J., CHOI, J. W., MOON, M.-W., LEE, K.-R., CHANG, Y. S., LEE, D.-Y. & KIM, H.-Y. 2015 Wicking and flooding of liquids on vertical porous sheets. *Phys. Fluids* **27** (3), 032105.
- KOTCHAPHAKEE, P. & WILLIAMS, M. C. 1970 Enhancement of nucleate pool boiling with polymeric additives. *Int. J. Heat Mass Transf.* **13** (5), 835–848.
- KOZENY, J. 1927 Uber kapillare leitung der wasser in boden. *Royal Academy of Science, Vienna, Proc. Class* **136**, 271–306.
- LANDERYOU, M., EAMES, I. & COTTENDEN, A. 2005 Infiltration into inclined fibrous sheets. *J. Fluid Mech.* **529**, 173–193.
- LI, J., ILLEPERUMA, W. R. K., SUO, Z. & VLASSAK, J. J. 2014 Hybrid hydrogels with extremely high stiffness and toughness. *ACS Macro Lett.* **3** (6), 520–523.
- LI, L., GAO, S., HAO, M., YANG, X., FENG, S., LI, L., WANG, S., XIONG, Z., SUN, F., LI, Y., BAI, Y., ZHAO, Y., WANG, Z. & ZHANG,

REFERENCES

- T. 2021 A novel, flexible dual-mode power generator adapted for wide dynamic range of the aqueous salinity. *Nano Energy* **85**, 105970.
- LIN, G., CHANG, S., KUO, C.-H., MAGDA, J. & SOLZBACHER, F. 2009 Free swelling and confined smart hydrogels for applications in chemomechanical sensors for physiological monitoring. *Sens. Actuators B Chem.* **136** (1), 186–195.
- LIU, X., STEIGER, C., LIN, S., PARADA, G. A., LIU, J., CHAN, H. F., YUK, H., PHAN, N. V., COLLINS, J., TAMANG, S., TRAVERSO, G. & ZHAO, X. 2019 Ingestible hydrogel device. *Nat. Commun.* **10** (1), 493.
- LOPES, C. M., BETTENCOURT, C., ROSSI, A., BUTTINI, F. & BARATA, P. 2016 Overview on gastroretentive drug delivery systems for improving drug bioavailability. *Int. J. Pharm.* **510** (1), 144–158.
- LUCAS, R. 1918 Ueber das zeitgesetz des kapillaren aufstiegs von flüssigkeiten. *Kolloid-Zeitschrift* **23** (1), 15–22.
- MAH, C. H., WU, Q. & DEEN, G. R. 2018 Effect of nature of chemical crosslinker on swelling and solubility parameter of a new stimuli-responsive cationic poly(n-acryloyl-n'-propyl piperazine) hydrogel. *Polym. Bull.* **75** (1), 221–238.
- MANGLIK, R. M., WASEKAR, V. M. & ZHANG, J. 2001 Dynamic and equilibrium surface tension of aqueous surfactant and polymeric solutions. *Exp. Therm. Fluid Sci.* **25** (1), 55–64.
- MAO, N. & RUSSELL, S. J. 2008 Capillary pressure and liquid wicking in three-dimensional nonwoven materials. *J. Appl. Phys.* **104** (3), 034911.
- NAVARRO-LUPIÓN, F.-J., BUSTAMANTE, P. & ESCALERA, B. 2005 Relationship between swelling of hydroxypropylmethylcellulose and the hansen and karger partial solubility parameters. *J. Pharm. Sci.* **94** (7), 1608–1616.

REFERENCES

- NELSON, W. R. & BAVER, L. D. 1941 Movement of water through soils in relation to the nature of the pores. *Soil Sci. Soc. Am. J.* **5**, 69–76.
- OLATUNJI, O. 2015 *Natural polymers: industry techniques and applications*. Springer.
- PROBSTEIN, R. F. 2005 *Physicochemical hydrodynamics: an introduction*. John Wiley & Sons.
- PURCELL, W. R. 1949 Capillary pressures - their measurement using mercury and the calculation of permeability therefrom. *J. Pet. Technol.* **1** (02), 39–48.
- PUTHIARAJ, P., LEE, Y.-R., ZHANG, S. & AHN, W.-S. 2016 Triazine-based covalent organic polymers: design, synthesis and applications in heterogeneous catalysis. *J. Mater. Chem. A* **4** (42), 16288–16311.
- RAUX, P. S., COCKENPOT, H., RAMAIOLI, M., QUÉRÉ, D. & CLANET, C. 2013 Wicking in a powder. *Langmuir* **29** (11), 3636–3644.
- RODRIGUEZ, E., GIACOMELLI, F. & VAZQUEZ, A. 2004 Permeability-porosity relationship in rtm for different fiberglass and natural reinforcements. *J. Compos. Mater* **38** (3), 259–268.
- ROSE, W. & WITHERSPOON, P. A. 1956 *Studies of wateflood performance*. Division of the Illinois state Geological Survey.
- RUBINSTEIN, M., COLBY, R. H. & ... 2003 *Polymer physics*, , vol. 23. Oxford university press New York.
- DE RUIJTER, M., HRYNEVICH, A., HAIGH, J. N., HOCHLEITNER, G., CASTILHO, M., GROLL, J., MALDA, J. & DALTON, P. D. 2018 Out-of-plane 3d-printed microfibers improve the shear properties of hydrogel composites. *Small* **14** (8), 1702773.
- SCHEIDEGGER, A. E. 1958 The physics of flow through porous media. *Soil Sci.* **86** (6), 355.

REFERENCES

- SHIN, B., HA, J., LEE, M., PARK, K., PARK, G. H., CHOI, T. H., CHO, K.-J. & KIM, H.-Y. 2018 Hygrobot: A self-locomotive ratcheted actuator powered by environmental humidity. *Sci. Robot.* **3** (14).
- SINGH, B. N. & KIM, K. H. 2000 Floating drug delivery systems: an approach to oral controlled drug delivery via gastric retention. *J. Control. Release* **63** (3), 235–259.
- SUJJA-AREEVATH, J., MUNDAY, D. L., COX, P. J. & KHAN, K. A. 1998 Relationship between swelling, erosion and drug release in hydrophilic natural gum mini-matrix formulations. *Eur. J. Pharm. Sci.* **6** (3), 207–217.
- SZYMCZAK, P. & LADD, A. J. C. 2011 Instabilities in the dissolution of a porous matrix. *Geophys. Res. Lett.* **38** (7).
- TESTONI, G. A., KIM, S., PISUPATI, A. & PARK, C. H. 2018 Modeling of the capillary wicking of flax fibers by considering the effects of fiber swelling and liquid absorption. *J. Colloid Interface Sci.* **525**, 166–176.
- THIRUMALESHWAR, M. 2006 *Fundamentals of Heat and Mass Transfer*. London: Pearson Education.
- THOMAS, S. W., CHIECHI, R. C., LAFRATTA, C. N., WEBB, M. R., LEE, A., WILEY, B. J., ZAKIN, M. R., WALT, D. R. & WHITESIDES, G. M. 2009 Infochemistry and infofuses for the chemical storage and transmission of coded information. *PNAS* **106** (23), 9147–9150.
- TWIST, J. N. & ZATZ, J. L. 1988 Membrane-solvent-solute interaction in a model permeation system. *J. Pharm. Sci.* **77** (6), 536–40.
- VARGHESE, J. S., CHELLAPPA, N. & FATHIMA, N. N. 2014 Gelatin–carrageenan hydrogels: role of pore size distribution on drug delivery process. *Colloids Surf. B* **113**, 346–351.

REFERENCES

- VRENTAS, J. S. & DUDA, J. L. 1979 Molecular diffusion in polymer solutions. *AIChE J.* **25** (1), 1–24.
- WAGGONER, R. A., BLUM, F. D. & LANG, J. C. 1995 Diffusion in aqueous solutions of poly(ethylene glycol) at low concentrations. *Macromolecules* **28** (8), 2658–2664.
- WASHBURN, E. W. 1921 The dynamics of capillary flow. *Phys. Rev.* **17** (3), 273–283.
- WERZER, O., WARR, G. G. & ATKIN, R. 2011 Compact poly (ethylene oxide) structures adsorbed at the ethylammonium nitrate- silica interface. *Langmuir* **27** (7), 3541–3549.
- WU, F., PANG, Y. & LIU, J. 2020 Swelling-strengthening hydrogels by embedding with deformable nanobarriers. *Nat. Commun.* **11** (1), 4502.
- WU, J., XU, F., LI, S., MA, P., ZHANG, X., LIU, Q., FU, R. & WU, D. 2019 Porous polymers as multifunctional material platforms toward task-specific applications. *Adv. Mater.* **31** (4), 1802922.
- XIA, L.-W., XIE, R., JU, X.-J., WANG, W., CHEN, Q. & CHU, L.-Y. 2013 Nano-structured smart hydrogels with rapid response and high elasticity. *Nat. Commun.* **4** (1), 2226.
- XIANG, S.-L., SU, Y.-X., YIN, H., LI, C. & ZHU, M.-Q. 2021 Visible-light-driven isotropic hydrogels as anisotropic underwater actuators. *Nano Energy* **85**, 105965.
- XU, X.-D., ZHANG, X.-Z., YANG, J., CHENG, S.-X., ZHUO, R.-X. & HUANG, Y.-Q. 2007 Strategy to introduce a pendent micellar structure into poly(*n*-isopropylacrylamide) hydrogels. *Langmuir* **23** (8), 4231–4236.
- YAN, H., FUJIWARA, H., SASAKI, K. & TSUJII, K. 2005 Rapid swelling/collapsing behavior of thermoresponsive poly(*n*-isopropylacrylamide) gel containing poly(2-(methacryloyloxy)decyl phosphate) surfactant. *Angew. Chem. Int.* **44** (13), 1951–1954.

REFERENCES

- YAN, Q. & HOFFMAN, A. S. 1995 Synthesis of macroporous hydrogels with rapid swelling and deswelling properties for delivery of macromolecules. *Polymer* **36** (4), 887–889.
- YANG, G.-Z., BELLINGHAM, J., DUPONT, P. E., FISCHER, P., FLORIDI, L., FULL, R., JACOBSTEIN, N., KUMAR, V., MCNUTT, M., MERRIFIELD, R. & ... 2018 The grand challenges of science robotics. *Sci. Robot.* **3** (14), eaar7650.
- YOON, J., CAI, S., SUO, Z. & HAYWARD, R. C. 2010 Poroelastic swelling kinetics of thin hydrogel layers: comparison of theory and experiment. *Soft Matter* **6** (23), 6004–6012.
- YUASA, H., TAKASHIMA, Y. & KANAYA, Y. 1996 Studies on the development of intragastric floating and sustained release preparation. i. application of calcium silicate as a floating carrier. *Chem. Pharm. Bull.* **44** (7), 1361–1366.
- ZENG, Y., ZOU, R. & ZHAO, Y. 2016 Covalent organic frameworks for co₂ capture. *Adv. Mater.* **28** (15), 2855–2873.
- ZHAN, X., CHEN, Z. & ZHANG, Q. 2017 Recent progress in two-dimensional cofs for energy-related applications. *J. Mater. Chem. A* **5** (28), 14463–14479.
- ZHANG, H., XI, S., HAN, Y., LIU, L., DONG, B., ZHANG, Z., CHEN, Q., MIN, W., HUANG, Q., LI, Y. & ... 2018a Determining electrospun morphology from the properties of protein–polymer solutions. *Soft matter* **14** (18), 3455–3462.
- ZHANG, W., ZHAO, Q. & YUAN, J. 2018b Porous polyelectrolytes: The interplay of charge and pores for new functionalities. *Angew. Chem. Int.* **57** (23), 6754–6773.
- ZHANG, Y. & RIDUAN, S. N. 2012 Functional porous organic polymers for heterogeneous catalysis. *Chem. Soc. Rev.* **41** (6), 2083–2094.

REFERENCES

- ZHENG, Z., WANG, H., DONG, L., SHI, Q., LI, J., SUN, T., HUANG, Q. & FUKUDA, T. 2021 Ionic shape-morphing microrobotic end-effectors for environmentally adaptive targeting, releasing, and sampling. *Nat. Commun.* **12** (1), 411.
- ZHOU, J. & WANG, B. 2017 Emerging crystalline porous materials as a multifunctional platform for electrochemical energy storage. *Chem. Soc. Rev.* **46** (22), 6927–6945.
- ZHU, L., QIU, J. & SAKAI, E. 2017 A high modulus hydrogel obtained from hydrogen bond reconstruction and its application in vibration damper. *RSC Adv.* **7** (69), 43755–43763.
- ZOU, L., SUN, Y., CHE, S., YANG, X., WANG, X., BOSCH, M., WANG, Q., LI, H., SMITH, M., YUAN, S. & OTHERS 2017 Porous organic polymers for post-combustion carbon capture. *Adv. Mater.* **29** (37), 1700229.

국 문 초 록

다공성 고분자의 팽창 및 용해 역학

서울대학교 대학원

기계항공공학부

정 소 현

요 약

수많은 단위체의 공유결합으로 이루어진 고분자 물질은 그 단위체의 종류에 따라 다양한 물리화학적 성질을 가질 수 있다. 이러한 물성의 다양성 및 조절 가능성 덕분에 현대 사회에서 고분자 물질은 매우 많은 산업 분야에서 활용되고 있다. 최근 생체 의학, 소프트 로봇 공학, 그리고 에너지 분야에 관한 관심이 증대되고, 이와 더불어 화석 연료의 고갈 및 환경 문제가 인류의 생존과 발전에 심각한 위협으로 계속해서 대두되면서 각 응용 분야에서 요구하는 물성을 지닌 친환경 기능성 고분자에 관한 연구에 대한 중요성이 두드러지고 있다. 다공성 구조는 부피 대비 넓은 표면적, 개방형 채널 및 기공 환경에 대한 높은 제어 가능성이라는 고유한 특성을 갖는다. 이러한 특성 덕분에 다공성 고분자는 물리적인 방식으로 재료의 물성이 제어될 수 있으며 이는 최근 몇 년

동안 수행된 대규모 연구로 입증된 바 있다. 즉, 다공성 구조는 친환경적인 방식으로 응용 분야에서 고분자에 요구하는 기능을 부과하거나 성능을 향상시킬 수 있다.

다공성 고분자는 수처리, 제약 산업, 식품 산업, 합성 화학, 이온 교환 수지 등에 사용되기 시작해 상용 리튬 이온 배터리와 슈퍼캐패시터에서 주요한 역할을 하는 분리막으로 상용 범위를 넓혀갔다. 또한 이러한 다공성 고분자는 에너지 저장, 액추에이터, 센서, 제어 약물 전달 분야, 가스 흡착 및 포집, 분자 분리, 촉매 작용 분야에서 높은 활용도를 가지고 있다고 전망되고 있다. 다양한 응용 분야에서 많은 경우 다공성 고분자는 액체에 노출되고 이로 인해 여러가지 물리화학적 현상이 발생한다. 그 중 용해 현상은 제어 약물 전달 및 오염 제거 분야에서 주요하게 제어되어야 할 현상이며 센서에도 응용이 가능하므로 그 중요도가 매우 높다. 또한 팽창 현상은 다공성 고분자의 부피를 변형시켜 움직임을 만들어 낼 수 있기 때문에 적절한 제어를 통해 액추에이터에서 원하는 움직임을 구현할 수 있고, 팽창을 통해 이를 유발하는 물질을 감지하는 센서로도 활용이 가능하여 이 또한 높은 중요도를 갖는다. 이러한 다공성 고분자의 용해 및 팽창 현상을 응용한 기술을 개발하고 해당 기술의 성능 개선을 위해서는 이 현상들에 대한 근본적인 이해가 선행되어야 한다. 그러나 다공성 구조의 복잡성에 의해 변형을 하지 않는 단순한 구조의 다공성 매질 내에서의 액체 거동에 대한 물리적 원리에 대한 연구만이 수행되어왔다. 최근 들어서야 다양한 스케일의 기공을 갖는 다공성 매질이나 변형이 가능한 다공성 매질과 같이 복잡한 다공성 매질 내에서의 액체 거동에 대한 물리적 원리 규명이 이루어지고 있으나 아직 미미한 수준이다. 특히 다공성 고분자의 용해 및 팽창 현상에서 액체는 다공성 고분자와 반응하여 다공성 고분자의 부피 팽창 및 상

변화를 유발하기 때문에 이에 대한 역학적 해석은 더욱 어렵다. 본 연구에서는 액체에 의한 다공성 고분자 팽창과 용해 메커니즘을 규명하고 이에 대한 정량적인 분석을 수행하였다. 이러한 분석을 바탕으로 물리적인 방법으로 다공성 고분자의 변형을 제어하거나 이를 활용하는 시스템을 개발하였다.

먼저 다공성 고분자의 팽창 메커니즘을 파악하고 이에 대한 이해를 바탕으로 팽창 현상을 응용한 시스템 설계 연구를 진행하였다. 구체적으로 친수성 고분자 사슬 사이에 많은 양의 수분을 구조체의 파괴 없이 저장할 수 있는 하이드로젤 중 하나인 전기감응성 하이드로젤의 팽창 역학을 전기장이 있을 때와 없을 때에 대해 이론 및 실험적으로 분석하였다. 여기서 전기감응성 하이드로젤은 액체와 접촉 시 고분자 사슬에서 이온이 해리되어 고분자 사슬은 전하를 띠는 젤을 의미한다. 전기장이 없는 경우 전기감응성 하이드로젤의 팽창 현상을 관찰하였고 그 속도가 매우 느리고 이는 삼투압에 의한 물 분자의 확산성 거동에 의해 발생한다는 것을 확인하였다. 반면에 전기장이 있는 경우 전기감응성 하이드로젤의 팽창 속도가 훨씬 빠르고 더 큰 팽창 비율을 갖는 것을 확인하였다. 이는 삼투압에 의한 유동에 전기장에 의해 유도되는 전기 삼투에 의한 유동까지 더해져 젤 내로 큰 유동이 발생하기 때문인 것을 정량적인 분석을 통해 확인하였다. 여기서 전기 삼투는 전해질 용액으로 채워진 다공성 매질에 전기장이 가해졌을 때 발생하는 유동이어서 전기장이 있는 경우 젤의 팽창 속도는 전기장의 세기에 비례하여 증가하며 이는 젤의 팽창 비율 및 두께에 의존하지 않고 일정하다. 또한 전기장이 있는 경우에 젤이 더 큰 팽창 비율을 갖는 원인은 전기장에 고분자 사슬의 신장 한계가 증가하기 때문인 것을 확인하였고 신장 한계가 포화 상태에 이르는 전기장의 세기의 임계값을 이론적으로 도출하였다. 이를 토대로 이러한 전기감응성 하이드로젤의 크고

빠른 팽창을 물리적인 구조체를 통해 내부 응력으로 변환하여 활용하는 시스템을 설계하였다. 구체적으로 전기감응성 하이드로젤을 높은 강성을 지니는 한정된 부피의 반투과성 막으로 감싸 시스템을 제작하였다. 여기서 사용된 막은 하이드로젤 내로의 액체의 투과는 허용하면서 하이드로젤의 팽창을 저해하여 젤 내부에 응력이 생성되도록 한다. 이러한 내부 응력은 하이드로젤의 강성을 증가시켜 변형에 대한 저항이 증가하여 큰 힘을 내거나 견딜 수 있게 한다. 이 때 전기감응성 하이드로젤의 팽창 역학을 바탕으로 하이드로젤 시스템에서 발생하는 힘에 대한 수학적 모델을 도출하였고 이를 실험과 비교하여 그 타당성을 입증하였다. 도출한 수학 모델로부터 하이드로젤 시스템의 주요 설계 변수를 도출하였으며, 시스템으로부터 발생 가능한 최대 힘을 이론적으로 예측하였다. 본 연구에서 제안한 하이드로젤 시스템은 하이드로젤이 고유하게 갖는 느린 반응성 및 압축력에 취약한 특성을 극복하여 큰 힘을 내는 빠른 액추에이터로서의 활용 가능성을 보였다는데 그 의의가 있고 이는 수중 건축물 혹은 해난 구조용 장비 제작에 사용될 수 있을 것으로 기대된다.

다음으로 다공성 고분자에서 용해를 동반한 액체의 거동 메커니즘을 파악하고 이를 바탕으로 다공성 고분자의 물리적인 미세 구조 제어를 통해 이를 제어하는 기술을 개발하는 연구를 진행하였다. 구체적으로 폴리에틸렌 수용액을 전기 방사하여 제작한 섬유 구조의 다공성 고분자 내에서의 액체의 거동을 정량적으로 분석하고 이에 대한 이론 모델을 도출하였다. 이 때, 고분자에 대한 액체의 용해도에 따라 액체의 종류를 비 용매, 부분 용매, 완전 용매로 구분하고 각각의 거동을 분석하였다. 비용매는 다공성 고분자를 용해시키지 않는 액체로 다공성 고분자 내에서의 거동은 표면 장력에 의해 발생하는 모세관 유동이며 다공성 매질 내에서의 액체의 거동에 대한 경험 식인 달시의

법칙을 잘 따르는 것을 확인하였다. 부분 용매는 용해도가 낮아 다공성 고분자의 일부만 용해시키기 때문에 다공성 고분자의 구조체는 유지되며 유동이 발생한다. 이러한 부분 용매의 거동을 관찰한 결과 이 또한 모세관 유동으로 비 용매와 유사하게 확산성 거동을 보이나 그 속도가 달시의 법칙으로 예측된 것에 비해 현저하게 느린 것을 확인하였다. 이러한 부분 용해성 모세관 유동의 속도에 대한 수학적 모델을 도출하기 위해 속도에 영향을 줄 수 있는 다공성 매질 및 액체에서의 변수를 추정하고 해당 변수들에 대한 용해의 영향력을 실험적으로 확인하였다. 그 결과, 고분자의 용해에 의한 용매 속 고분자 농도 증가에 의한 용매의 점도 증가가 부분 용해성 모세관 유동의 느린 속도에 가장 큰 원인임으로 확인하였다. 완전 용매는 높은 용해도를 갖는 용매로 다공성 고분자와 접촉 시 이를 전부 용해시켜 유동이 발생할 때 구조체가 아주 짧은 시간만 유지된다. 다공성 고분자 내에서 이러한 완전 용매의 유동은 비 용매와 부분 용매의 거동과는 다르게 일정한 속도로 발생되는 것을 관찰하였다. 이때 침투한 완전 용매의 침단 계면이 가지 형태로 매우 불규칙하게 나타나는 것을 확인하였다. 이러한 완전 용매의 유동 매커니즘을 파악하기 위해 다양한 스케일에서 완전 용매 유동을 가시화하였고 그 결과 다공성 고분자의 용해 과정 중에 고분자의 팽창에 의해 겔 층이 형성되는 것을 확인하였다. 이러한 겔 층은 기공의 폐쇄를 야기하여 기공을 통한 용매의 모세관 유동을 억제하지만 이는 고분자의 용해를 통해 사라져 다시금 기공이 생성되고 이를 통한 용매의 모세관 유동이 재개된다. 따라서 다공성 고분자 내 완전 용매의 거동은 기공의 폐쇄 및 재개에 의한 짧은 거리의 모세관 유동의 반복 과정이라고 할 수 있다. 이를 토대로 다공성 고분자 내에서의 완전 용매의 거동에 대한 이론 모델을 도출하였으며 실험적으로 그 타당성을 입증하였다. 도출한 이론 모델의 전체

조건으로부터 다공성 고분자 내에서의 완전 용매의 유동 발생 조건이 다공성 고분자의 물리적인 미세 구조에 따른 용매의 확산성에 의해 결정된다는 것을 이론적으로 발견하였다. 용매의 확산성이 좋은 구조의 경우 기공을 막는 젤 층이 지속적으로 성장 가능하여 기공의 재생성이 발생할 수 없다. 따라서 다공성 고분자의 미세 구조 제어를 통해 완전 용매의 유동 방향을 제어할 수 있고 다공성 고분자의 용해 속도를 제어할 수 있다. 이를 확인하기 위해 방향성 있는 전기 방사를 통해 섬유들이 한 방향으로 잘 정렬된 구조를 갖는 다공성 고분자를 제작하였고 여기서 완전 용매의 유동을 관찰한 결과 용매의 확산성이 낮은 방향인 섬유를 가로지르는 방향으로만 유동이 발생하는 것을 확인하였다. 이러한 다공성 고분자의 물리적인 미세 구조 제어를 통한 용해 방향 및 속도 제어 기술은 투약 속도 정밀 제어 약물 전달 시스템 설계, 센서, 그리고 주변 환경에 대해 반응하여 변형하는 소프트 로봇을 고안에 도움을 줄 수 있을 것으로 기대된다.

본 연구는 액체에 의한 다공성 고분자의 변형 역학에 대해 분석하고 이를 물리적인 방법으로 응용 및 제어하는 시스템을 설계하여 친환경적인 방법으로 다공성 고분자의 물성을 제어했다는 데 그 의의가 있다. 이는 고분자 응용 기술 개발 및 성능 개선 방법에 새로운 패러다임을 제시했다고 할 수 있다. 또한 전기감응성 하이드로젤 내에서의 유동 해석은 슈퍼커패시터의 저항의 정량적인 분석 및 이를 결정하는 인자들 도출에 도움을 줄 수 있고 다공성 고분자 내에서의 용매의 거동에 대한 해석은 고분자 필터 투과 유동 및 필터의 오염 물질 제거에 필요한 설계 변수 도출에 도움을 줄 수 있다. 또한 하이드로젤의 팽창을 내부 응력으로 변환하여 이를 통해 힘을 발생하는 시스템은 용액의 농도나 용액 내 전기장의 유무 및 그 세기를 측정하는 센서로 활용할 수 있다.

따라서 본 연구의 결과들은 다공성 고분자의 응용 분야에 적용될 수 있으므로 활용도가 높다고 할 수 있다.

주요어 : 고분자, 다공성 물질, 팽창, 용해, 모세관 유동

학 번: 2015-22723